



Full length article

Finite strain phase-field microelasticity theory for modeling microstructural evolution

Pengyang Zhao^{*a,b}, Thaddeus Song En Low^c, Yunzhi Wang^b, Stephen R. Niezgod^{b,d}

^a Department of Engineering Mechanics, School of Naval Architecture, Ocean & Civil Engineering, Shanghai Jiao Tong University, 800 Dongchuan Road, Shanghai, 200240, China

^b Department of Materials Science and Engineering, The Ohio State University, 2041 College Road, Columbus, OH 43210, USA

^c ANSYS Inc., 1794 Olympic Parkway, Park City, UT 84098, USA

^d Department of Mechanical and Aerospace Engineering, The Ohio State University, 201 W. 19th Avenue, Columbus, OH 43210, USA



ARTICLE INFO

Article History:

Received 13 October 2019

Revised 18 March 2020

Accepted 22 March 2020

Available online 8 April 2020

Keywords:

Twinning
Micromechanics
Microstructures
Spectral method
Computer simulation

ABSTRACT

Implementing the phase-field model at finite strains is usually considered unattainable through the spectral method, largely because of the nonlinearity in the transformation-induced microelasticity. Here we present a phase-field microelasticity (PFM) theory at finite strains with a representation in the reference configuration, allowing the spectral method to be readily incorporated. Following the spirit of Khachaturyan's PFM theory at small strains, the elastic energy is formulated as a functional of microstructure (order parameters) solely, which should automatically satisfy the mechanical equilibrium. Thermodynamic consistency of the current theory under multiplicative decomposition of the total deformation gradient (into elastic and inelastic parts) and in conjunction with hyperelasticity and the time-dependent Ginzburg-Landau equation is shown rigorously. The new theory is first applied to the classical Eshelby's inclusion problem, where shear-dilatation coupling due to geometric nonlinearity is shown and a convergence study between small strain and finite strain theories is also carried out. The effects of geometric nonlinearity on the co-evolution of micromechanics and microstructure is further studied through modeling the growth of $\{1\ 0\ \bar{1}\ 2\}$ $(\bar{1}\ 0\ 1\ 1)$ deformation twins in magnesium. The simulation results suggest significant differences in terms of the shape of and the stress field around the deformation twin. In particular, the current finite strain PFM theory predicts a deviation of the twin boundary plane from the theoretical K_1 plane, which is not captured in the small strain theory nor in the crystallographic theory. A parametric study further reveals that the observed deviation is caused by the tip effect of the finite-sized twin plate when the aspect ratio is relatively small. The symmetry of the stress field distribution around the twin tip is also found to be drastically different between the small strain and finite strain based phase-field modeling. The sharp twin tip observed in experiments is also shown to be likely related to the anisotropy in twin/matrix interface mobility.

© 2020 Acta Materialia Inc. Published by Elsevier Ltd. All rights reserved.

1. Introduction

Alloy design is largely concerned with microstructure design that requires the ability to predict the evolution of microstructure in an alloy during processing and in service. For structural materials, the efforts have been focused on controlling certain microstructural attributes to regulate dislocation activities, grain boundary migration, crack initiation/propagation, etc., and thus to tailor the microstructure-property relationship. The microstructure of an alloy is defined by a collection of chemical and structural non-uniformities, including concentration variation, impurity segregation, dislocations, homo/hetero-phase interfaces, surfaces, cracks, and voids. These non-uniformities are described in the phase-field (PF) method by order

parameters (OPs), representing non-mechanical variables apart from the stress and strain.

In situations where the variation of external (mechanical and/or thermal) loads can be considered static or quasi-static as compared to the propagation of elastic waves, the mechanical variables may reach an equilibrium much faster than these non-mechanical ones. This inherent *time scale separation* implies that it is no longer necessary to treat the mechanical and non-mechanical variables on the same footing. Instead, the latter can be considered as “fixed” at an instant of (simulation) time and the resulting stress and displacement then become “slave” variables, which are determined by directly solving the mechanical equilibrium without explicitly considering their time evolution. This is the fundamental idea behind Khachaturyan's seminal phase-field microelasticity (PFM) theory [1], which has been continuously developed in the past few decades as a foundation for studying microstructure evolution during phase transformations and deformation in solids [2,3].

* Corresponding author.

E-mail address: zhao.py@sjtu.edu.cn (P. Zhao).

However, the resulting models mainly adopt the original small strain formulation and thus ignore the geometric nonlinearity involved in phase transformations and plastic deformation, which can be critical in cases such as martensite transformation, deformation twinning, and plastic deformation.

PF models incorporating the finite strain theory have been developed since the past decade. For example, [4–6] developed PF models for displacive transformations and [7] developed a PF model coupled with crystal plasticity at finite strains for deformation twinning. [8] also developed a finite strain PF model to address the inertia effect during martensite transformation. However, these models are formulated for and implemented in the conventional finite-element or finite-difference methods, which are well known to be orders of magnitude slower than the spectral method [9], as demonstrated, in particular, in the application to micromechanics of solids [10,11]. In a different approach, [12] divided the finite strain into a series of small deformation processes and then used a hypoelasticity model, allowing solutions from the geometrically linearized problem to be used with a spectral method based implementation. While this method guarantees high numerical efficiency, the use of hypoelasticity implies that it is not consistent with thermodynamics.

In addition, the existing finite strain models incorporating microstructures mainly follow the classical idea by starting with the fundamental balance laws and thermodynamics, which lead to a set of rate equations describing the time evolution of both mechanical and non-mechanical variables [4,6,8,13–15]. A common feature of these models is that an elastic energy density is directly used to derive a completely localized driving force for the microstructure evolution. However, it is well known that the elastic energy in a heterogeneously transformed solid contains self-interaction [1] and is essentially a convolution integral owing to the underlying non-local nature. Although in certain cases the derivative of the integral elastic energy with respect to a parameter may be localized [16], this is not a general law and thus a rigorous derivation is still needed for the given problem. As a result, the use of an elastic energy density rather than the integral elastic energy is not justified. In fact, since the stress satisfying the mechanical equilibrium is a functional of the OP in PF theory [1], the integral elastic energy thus becomes a functional of a functional and the resulting functional derivative with respect to the OP should in general adopt an integral form as shown in Appendix A.

The purpose of the current paper is twofold: (i) to develop a phase-field microelasticity theory at finite strains with a representation in the reference configuration, allowing the spectral method based micromechanical solvers to be readily incorporated; (ii) to benchmark the effect of geometric nonlinearity using examples that are simple but representative to modeling the micromechanical and microstructural evolution in solids. In particular, the development of our new theory follows the spirit of [1] to take the advantage of time scale separation between mechanical and microstructural variables as discussed previously. Two benchmark problems, i.e., Eshelby's inclusion and deformation twinning, are solved using both the small strain and finite strain models. The former problem involves solving the static micromechanical field of a given microstructure, whereas the latter one represents the co-evolution of micromechanical and microstructural variables typically found in many thermal-mechanical processes of solids.

2. Theory

2.1. Kinematics under multiplicative decomposition

We start with a function of motion, $\chi(\mathbf{X}) : \mathfrak{B}_0 \rightarrow \mathbb{R}^3$, which maps any point \mathbf{X} (material point) of the body in the reference (initial) configuration \mathfrak{B}_0 to a spatial (current configuration) point \mathbf{x} in the 3D Euclidean space \mathbb{R}^3 . The total deformation gradient is defined as

$$\mathbf{F} \equiv \frac{\partial \chi}{\partial \mathbf{X}} = \nabla_{\mathbf{X}} \chi. \quad (1)$$

\mathbf{F} is then assumed to follow the multiplicative decomposition

$$\mathbf{F} = \mathbf{F}_e \mathbf{F}_i, \quad (2)$$

$$j_e \equiv \det \mathbf{F}_e > 0, \quad j_i \equiv \det \mathbf{F}_i > 0,$$

where \mathbf{F}_i is the net effect due to all the inelastic deformation modes and \mathbf{F}_e is the elastic deformation. In specific applications, \mathbf{F}_i can be either plastic deformation $\mathbf{F}_i = \mathbf{F}_p$ [17] or structural transformation $\mathbf{F}_i = \mathbf{F}_t$ [18], or a combination of both $\mathbf{F}_i = \mathbf{F}_t \mathbf{F}_p$ [6]. Eq. (2) introduces an intermediate configuration that connects the reference and current configurations, as illustrated in Fig. 1. The positive determinants in Eq. (2) imply that \mathbf{F}_e and \mathbf{F}_i are invertible and physically admissible.

In finite strain theory, the deformation can be measured in any one of the configurations involved, i.e., the reference, intermediate, and current configurations in Fig. 1, which have been summarized in Table 1. While these different measures describe the same kinematics, the choice matters to the numerical implementation, e.g., “Total Lagrangian” vs. “Updated Lagrangian” formulations in nonlinear finite-element analysis. A primary goal of the current finite strain PFM theory is to develop the formalism in the reference configuration, which enables the usage of Fourier spectral method on a fixed regular grid throughout the entire deformation analysis. This requires that the final representation of our theory must be in terms of quantities all defined in the reference configuration.

It also needs to be pointed out that the additive decomposition relations listed in Table 1 are derived solely from the multiplicative decomposition (see Appendix B for the detailed derivation). In each of these relations, apart from two strain tensors that are defined in the usual Green-Lagrange and/or Euler-Almansi way in a given configuration, the third one is related to a strain tensor in a different configuration via appropriate push-forward and/or pull-back operations. As a result, they are different from the Green-Naghdi decomposition [19], which is a direct assumption in total analogy with the decomposition of total strain into elastic and plastic parts in the small strain theory.

2.2. Phase-field microelasticity at finite strains

At the highest level, the total Helmholtz free energy is partitioned into elastic and inelastic contributions

$$\Psi \equiv \Psi_e + \Psi_i \quad (3)$$

where the elastic part Ψ_e depends explicitly on \mathbf{F}_e (or equivalently \mathbf{E}_e) and the inelastic part Ψ_i depends on measures of the inelastic state described by the OP field in PF theory. In general, Ψ_i is explicitly formulated as a functional of both OP and the gradient of OP, whereas Ψ_e is by definition a functional of \mathbf{F}_e and thus depends on OP implicitly via the coupling between OP and \mathbf{F}_i . In the following, we first present the constitutive equations commonly used to describe the elastic and inelastic behaviors of solids and then show their thermodynamic consistency.

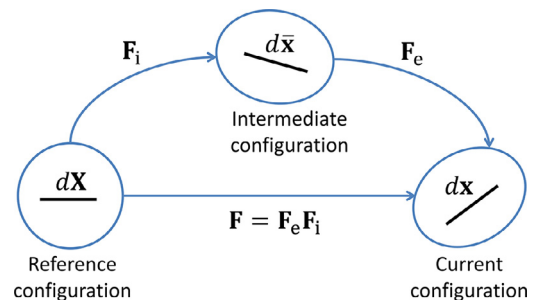


Fig. 1. Schematics of the multiplicative decomposition of the total deformation gradient \mathbf{F} into an inelastic deformation \mathbf{F}_i and elastic deformation \mathbf{F}_e , which bring the reference configuration successively into the intermediate and current configurations.

Table 1
Deformation measures in different configurations.

Configuration	Reference	Intermediate	Current
Right Cauchy-Green deformation tensor	$\mathbf{C} = \mathbf{F}^T \mathbf{F}$ $\mathbf{C}_i = \mathbf{F}_i^T \mathbf{F}_i$	$\bar{\mathbf{C}}_e = \mathbf{F}_e^T \mathbf{F}_e$	
Left Cauchy-Green deformation tensor		$\bar{\mathbf{b}}_i = \mathbf{F}_i \mathbf{F}_i^T$	$\mathbf{b} = \mathbf{F} \mathbf{F}^T$ $\mathbf{b}_e = \mathbf{F}_e \mathbf{F}_e^T$
Green-Lagrange strain tensor	$\mathbf{E} = \frac{1}{2}(\mathbf{C} - \mathbf{I})$ $\mathbf{E}_i = \frac{1}{2}(\mathbf{C}_i - \mathbf{I})$	$\bar{\mathbf{E}}_e = \frac{1}{2}(\bar{\mathbf{C}}_e - \mathbf{I})$	
Euler-Almansi strain tensor		$\bar{\mathbf{e}}_i = \frac{1}{2}(\mathbf{I} - \bar{\mathbf{b}}_i^{-1})$	$\mathbf{e} = \frac{1}{2}(\mathbf{I} - \mathbf{b}^{-1})$ $\mathbf{e}_e = \frac{1}{2}(\mathbf{I} - \mathbf{b}_e^{-1})$
Additive decomposition	$\mathbf{E}_e = \mathbf{E} - \mathbf{E}_i$ $\mathbf{E}_e \equiv \mathbf{F}_i^T \bar{\mathbf{E}}_e \mathbf{F}_i$ $\mathbf{E}_e \equiv \mathbf{F}_e^T \mathbf{e}_e \mathbf{F}_e$	$\bar{\mathbf{E}} = \bar{\mathbf{e}}_i + \bar{\mathbf{E}}_e$ $\bar{\mathbf{E}} \equiv \mathbf{F}_i^T \bar{\mathbf{E}}_e \mathbf{F}_i^{-1}$ $\bar{\mathbf{E}} \equiv \mathbf{F}_e^T \mathbf{e}_e \mathbf{F}_e^{-1}$	$\mathbf{e}_i = \mathbf{e} - \mathbf{e}_e$ $\mathbf{e}_i \equiv \mathbf{F}_e^{-T} \mathbf{E}_i \mathbf{F}_e^{-1}$ $\mathbf{e}_i \equiv \mathbf{F}_e^{-T} \bar{\mathbf{e}}_i \mathbf{F}_e^{-1}$

2.2.1. Elastic constitutive equations

Denoting ψ_e as the elastic strain energy density per unit mass, the elastic energy Ψ_e in Eq. (3) is formally written as

$$\Psi_e = \int_{V_0} \rho_0 \psi_e dV_0 = \int_V \rho \psi_e dV \quad (4)$$

where V and V_0 represent the volume of the space domain occupied by the current and reference configurations, respectively, and ρ and ρ_0 are the mass density in the corresponding configurations. Owing to the multiplicative decomposition of Eq. (2), the intermediate configuration is taken as the undeformed (“stress-free”) state, in which we formulate ψ_e using the hyperelasticity theory as

$$\bar{\rho} \psi_e = \frac{1}{2} \bar{\mathbf{E}}_e : \mathbb{C} : \bar{\mathbf{E}}_e, \quad \bar{\mathbf{S}} = \bar{\rho} \frac{\partial \psi_e}{\partial \bar{\mathbf{E}}_e} = \mathbb{C} : \bar{\mathbf{E}}_e \quad (5)$$

where \mathbb{C} is the elastic stiffness tensor and $\bar{\mathbf{S}}$ is the 2nd Piola-Kirchhoff (P-K) stress tensor defined in the intermediate configuration. Eq. (5) employs strain and stress measures associated with the intermediate configuration and their representations in the reference configuration are derived from the additive decomposition in Table 1, which leads to

$$\rho_0 \psi_e = \frac{j_i}{2} (\mathbf{F}_i^T \mathbf{E}_e \mathbf{F}_i^{-1}) : \mathbb{C} : (\mathbf{F}_i^T \mathbf{E}_e \mathbf{F}_i^{-1}) \quad (6)$$

$$\mathbf{S} \equiv \rho_0 \frac{\partial \psi_e}{\partial \mathbf{E}_e} = j_i \mathbf{F}_i^{-1} \cdot (\mathbb{C} : (\mathbf{F}_i^T \mathbf{E}_e \mathbf{F}_i^{-1})) \cdot \mathbf{F}_i^{-T} = j_i \mathbf{F}_i^{-1} \bar{\mathbf{S}} \mathbf{F}_i^{-T},$$

where we have defined a symmetric stress tensor \mathbf{S} that can be considered as the pull-back of $\bar{\mathbf{S}}$ to the reference configuration. Since the 2nd P-K stress is related to the Cauchy stress σ by $\bar{\mathbf{S}} = j_e \mathbf{F}_e^{-1} \sigma \mathbf{F}_e^T$, we can further obtain

$$\mathbf{S} = j_i j_e \mathbf{F}_i^{-1} \mathbf{F}_e^{-1} \sigma \mathbf{F}_e^T \mathbf{F}_i^{-T} = j \mathbf{F}^{-1} \sigma \mathbf{F}^{-T} \quad (7)$$

where $j = \det \mathbf{F} = j_i j_e$. Eq. (7) confirms that even under the multiplicative decomposition of Eq. (2), the stress measures defined above still exhibit formally the same relationship as in a pure elastic deformation. Note that in the above derivation, we ignore the deformation dependence of the elastic stiffness tensor, which is a common practice and considered reasonable as long as the defects population (i.e., vacancies) introduced by deformation is not significant enough to degrade the elastic modulus.

2.2.2. Inelastic constitutive equations

The definition of OP in finite strain PF theory should be configuration-dependent. We use η_0 and η to denote the OP field defined in the reference and current configurations, respectively. The connection between these quantities is derived based on the physical meaning of the OP. For instance, if the OP represents a conserved quantity, the connection should be similar to that between mass densities defined in different configurations. For a non-conserved OP of current interest, we require that the volume fraction of the underlying “ordering”, measured by the OP value, is independent of the

configuration, that is,

$$\frac{1}{V_0} \int_{V_0} \eta_0(\mathbf{X}) dV_0 = \frac{1}{V} \int_V \eta(\mathbf{x}) dV. \quad (8)$$

This implies that the overall transformation kinetics should be invariant under a configuration change. From Eq. (8) we have $\eta_0/V_0 = \det(\mathbf{F})(\eta/V) = (\rho_0 \eta)/(\rho V)$, where the quantity η_0/V_0 and η/V represent the volume density (associated with the transformed material) in the reference and current configurations, respectively. In addition, we assume that the spatial variation of density functions ρ_0 and ρ are small enough such that they can be considered as constant, which is generally valid in plasticity and phase transformations in solids when little voids and/or volume change are involved and leads to $\rho V = \rho_0 V_0$. Under these conditions, we obtain

$$\eta_0(\mathbf{X}) = \eta(\chi(\mathbf{X})), \quad (9)$$

which should be expected as how the kinematics is measured should not change the physical state (OP value) of the material. Once the OP is rigorously defined, we can proceed to formulate the inelastic energy Ψ_i in Eq. (3), which consists of two contributions, namely,

$$\Psi_i = \Psi_i^c + \Psi_i^g. \quad (10)$$

In Eq. (10), Ψ_i^c , the chemical free energy, is an integral of a local free energy density per unit mass ψ^c

$$\Psi_i^c = \int_{V_0} \rho_0 \psi^c dV_0 = \int_V \rho \psi^c dV, \quad (11)$$

and Ψ_i^g , the gradient energy, is formulated as

$$\Psi_i^g = \int_{V_0} \kappa_0 : (\nabla_x \eta_0 \otimes \nabla_x \eta_0) dV_0 = \int_V \kappa : (\nabla_x \eta \otimes \nabla_x \eta) dV, \quad (12)$$

where κ_0 and κ are second-rank tensors related to interfacial energies measured in the reference and current configurations, respectively. Eq. (12) requires that the total gradient energy must be invariant under a configuration change, which, combined with Eq. (9), leads to

$$\kappa = \frac{1}{j} \mathbf{F} \kappa_0 \mathbf{F}^T. \quad (13)$$

The experimentally measured interfacial energies are normally in the current configuration and can only be used to construct κ . Eq. (13) then serves as the pull-back from κ to obtain κ_0 . Note that if κ is symmetric, Eq. (13) ensures that κ_0 remains symmetric. However, if we have $\kappa = \kappa \mathbf{I}$, representing an interface with isotropic interfacial energy, Eq. (13) leads to

$$\kappa = \kappa \mathbf{I}, \quad \kappa_0 = j \kappa \mathbf{C}^{-1}. \quad (14)$$

An important consequence of Eq. (14) is that even though physically (in the current configuration) we have an interface with isotropic interfacial energy, an apparent interfacial anisotropy may still arise when formulating the gradient energy in the reference configuration. This is

understandable because anisotropic stretching along different directions may lead to non-zero off-diagonal components of \mathbf{C} in Eq. (14).

2.2.3. Time evolution of the order parameter

The time-dependent Ginzburg-Landau kinetic equation used by [20] is currently adopted and formulated in the reference configuration at finite strains, which gives the time evolution equation for a non-conserved OP

$$\dot{\eta}_0 = -M \frac{\delta \Psi}{\delta \eta_0} = -M \left(\frac{\delta \Psi_e}{\delta \eta_0} + \frac{\delta \Psi_i}{\delta \eta_0} \right) \quad (15)$$

where $M (>0)$ is a mobility constant. Note that Eq. (15) is considered here because a case study involving the non-conserved OP field will be carried out later in Section 4. For conserved OP fields, coupling the current PFM theory with Cahn-Hilliard equation can follow the similar way straightforwardly.

The elastic driving force $\delta \Psi_e / \delta \eta_0$ in Eq. (15) can be expressed in terms of the OP field together with some micromechanical variables, leading to the following formulation for general purposes

$$\frac{\delta \Psi_e}{\delta \eta_0(\mathbf{X})} = -\mathbf{F}_i^T \mathbf{CS} : \frac{d\mathbf{F}_i}{d\eta_0} \quad (16)$$

The derivation of Eq. (16) starts with the integral elastic energy and inevitably involves the use of the chain rule of a functional of a functional (Appendix A). (A rigorous derivation of Eq. (16) can be found in Appendix C.) Because of the geometric nonlinearity and material non-uniformity, it is likely impossible to obtain closed-form expressions associated with the mechanical fields at mechanical equilibrium, which only exist in the small strain version of PFM [1]. As a result, Eq. (16) essentially provides a simple expression in the reference configuration and the inherent long-range nature of elasticity is encapsulated in \mathbf{C} and \mathbf{S} , which should be obtained from solving the mechanical equilibrium. A spectral method for obtaining the equilibrium micromechanical fields required for Eq. (16) will be discussed in Section 3.1.

The inelastic driving force $\delta \Psi_i / \delta \eta_0$ in Eq. (15) generally contains the contributions of both the local chemical free energy ($\delta \Psi_i^c / \delta \eta_0$) and the non-local gradient energy term ($\delta \Psi_i^g / \delta \eta_0$) according to Eq. (10). Their actual forms depend on the specific problem in question and thus do not possess general expressions. Nevertheless, it will be shown next that the use of the Ginzburg-Landau equation (Eq. (15)) together with Eq. (16) always ensures the thermodynamic consistency.

2.2.4. Thermodynamic consistency

For purely mechanical scenarios where the temperature is constant and homogeneous, the dissipation rate per unit mass, \mathcal{D} , in the reference configuration adopts

$$\mathcal{D} = \frac{1}{\rho_0} \mathbf{P} : \dot{\mathbf{F}} - \frac{\partial \psi}{\partial t} \quad (17)$$

where $\mathbf{P} = \mathbf{F}\mathbf{S}$ is the 1st P-K stress tensor, $\dot{\mathbf{F}} = d\mathbf{F}/dt$, and ψ is the specific quantity (per unit mass) of the total Helmholtz free energy Ψ in Eq. (3). Plugging into Eq. (17) the multiplicative decomposition (Eq. (2)), together with the elastic and inelastic constitutive equations and the OP evolution equation discussed previously, it can be shown that

$$\mathcal{D} = \frac{M}{\rho_0} \left| \left(\mathbf{F}_i^T \mathbf{CS} - \frac{\delta \Psi_i}{\delta \mathbf{F}_i} \right) : \frac{d\mathbf{F}_i}{d\eta} \right|^2 \geq 0. \quad (18)$$

The non-negative dissipation rate suggests that the current finite strain PFM theory is consistent with the Clausius-Duhem inequality and hence thermodynamically consistent.

3. Model implementation and benchmark

The key to implementing the current PFM theory is to obtain the stress field satisfying the mechanical equilibrium for a given

microstructure. In previous finite strain PF models [4–6,8], the mechanical equilibrium is solved using finite-element or finite-difference methods. These traditional numerical solvers are known to be computationally expensive with lower accuracy as compared to the Fourier spectral method, which is shown by fundamental mathematical analysis [9] and also demonstrated in recent micromechanical simulations [10,11]. In the following, we will first present the key equations of Fourier spectral method by [10] for solving the mechanical equilibrium and then solve the micromechanical fields of a spherical Eshelby's inclusion at finite strains as a benchmark problem.

3.1. Spectral method solution of static equilibrium at finite strains

The micromechanical fields used in Eq. (16) are solutions of the static equilibrium plus a constitutive model

$$\begin{aligned} \nabla_{\mathbf{X}} \cdot \mathbf{P}(\mathbf{X}) &= \mathbf{0}, \\ \mathbf{P}(\mathbf{X}) &= \mathbf{P}(\mathbf{F}(\mathbf{X}), \mathbf{v}(\mathbf{X})), \end{aligned} \quad (19)$$

where \mathbf{v} is a vector field containing all the relevant internal variables. The spectral method for solving Eq. (19) starts with the decomposition

$$\boldsymbol{\chi}(\mathbf{X}) = \bar{\mathbf{F}}\mathbf{X} + \boldsymbol{\zeta}, \quad \text{with } \langle \boldsymbol{\zeta} \rangle = \mathbf{0} \quad (20)$$

where $\bar{\mathbf{F}}$ is the macroscopic (volume-average) deformation gradient, $\boldsymbol{\zeta}$ represents a periodic fluctuation and $\langle \cdot \rangle$ means the volume-average operator. This leads to the decomposition of the total deformation gradient

$$\mathbf{F} = \bar{\mathbf{F}} + \delta\mathbf{F}, \quad \text{with } \delta\mathbf{F} \equiv (\nabla \boldsymbol{\zeta})_{\mathbf{X}}. \quad (21)$$

Following the work of [21], we write the (generally nonlinear) constitutive model as

$$\mathbf{P}(\mathbf{X}) = \mathbb{A}\mathbf{F}(\mathbf{X}) + \boldsymbol{\tau}(\mathbf{X}) \quad (22)$$

where the first term represents the stress of a linear reference medium with a homogeneous stiffness \mathbb{A} and the second term characterizes the stress difference between the reference and the actual media, often called the ‘‘polarization field’’. Substituting Eqs. (20)–(22) into the static equilibrium of Eq. (19) and using the Fourier transform¹, we arrive at

$$\tilde{\mathbb{G}}(\mathbf{g}) \cdot \tilde{\boldsymbol{\zeta}}(\mathbf{g}) = \mathbf{i} \tilde{\boldsymbol{\tau}}(\mathbf{g}) \cdot \mathbf{g} \quad (23)$$

where $\tilde{\cdot}$ means the Fourier transform, $\mathbf{i} = \sqrt{-1}$, and \mathbf{g} is the reciprocal vector. The second-rank tensor \mathbb{G} is defined in Fourier space as $\tilde{\mathbb{G}}_{mn} \equiv \mathbb{A}_{mtns} g_t g_s$. Eq. (23) is the static equilibrium of Eq. (19) converted into the reciprocal space with the help of a linear reference medium (Eq. (22)). Being a set of algebraic equations, the solution of Eq. (23) can be simply written as

$$\tilde{\boldsymbol{\zeta}}(\mathbf{g}) = \begin{cases} \mathbf{0} & \text{for } \mathbf{g} = \mathbf{0} \\ \mathbf{i} \tilde{\mathbb{G}}^{-1} \cdot \tilde{\boldsymbol{\tau}} \cdot \mathbf{g} & \text{for } \mathbf{g} \neq \mathbf{0} \end{cases} \quad (24)$$

where the solution for $\mathbf{g} = \mathbf{0}$ is given by the requirement of $\langle \boldsymbol{\zeta} \rangle = \mathbf{0}$. Then the periodic fluctuation of the deformation gradient is given in the reciprocal space as

$$\delta \tilde{\mathbf{F}}(\mathbf{g}) = \begin{cases} \mathbf{0} & \text{for } \mathbf{g} = \mathbf{0} \\ \mathbf{i} \tilde{\boldsymbol{\tau}} & \text{for } \mathbf{g} \neq \mathbf{0} \end{cases} \quad (25)$$

where a fourth-rank tensor operator is defined in Fourier space as $\tilde{\Gamma}_{mnpq} \equiv -\tilde{\mathbb{G}}_{mp}^{-1} g_n g_q$. Note that $\tilde{\Gamma}$ is in fact the Green's function operator that relates the stress field ($\boldsymbol{\tau}$) to a deformation field ($\delta\mathbf{F}$). Since $\boldsymbol{\tau}$ depends on the stress field \mathbf{P} (Eq. (22)), which again depends on the deformation gradient field, Eq. (25) can only be solved in an iterative manner. In our current implementation, we adopt the basic scheme

¹ The Fourier transform of a real space function $f(\mathbf{X})$ is defined as $\tilde{f}(\mathbf{g}) = \int f(\mathbf{X}) \exp(-\mathbf{i}\mathbf{X} \cdot \mathbf{g}) d^3\mathbf{X}$. The inverse transform gives $f(\mathbf{X}) = (2\pi)^{-3} \int \tilde{f}(\mathbf{g}) \exp(\mathbf{i}\mathbf{X} \cdot \mathbf{g}) d^3\mathbf{g}$.

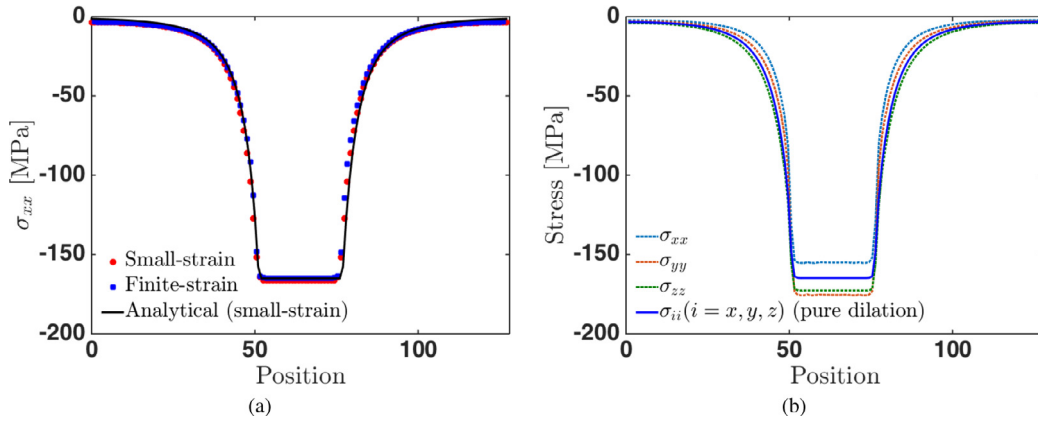


Fig. 2. (a) Predicted σ_{xx} along a probe line parallel to x -axis and across the center of the inclusion for the case of $\alpha = 0.2$, $\gamma = 0$. (b) Predicted diagonal stress components σ_{ii} along a probe line parallel to i -axis, where $i = x, y, z$, for the case of $\alpha = 0.2$, $\gamma = 0.2$.

presented in [10], where more details about the numerical aspects can be found. The significant computational advantage of the spectral method originates from the simple algebraic nature of the mechanical equilibrium equation in the reciprocal space (Eq. (23)) together with the $O(N \log N)$ efficiency offered by the *fast Fourier transform* algorithm.

3.2. A spherical Eshelby's inclusion as a benchmark

While the effect of geometric nonlinearity has been explored in some models, e.g., [8] and [4], the drastic difference between the results of the small strain theory (SST) and finite strain theory (FST) presented in these complex problems still urges applications to some simple but representative problems that can serve as a benchmark purpose. In addition, it is expected that SST and FST results should become indistinguishable to each other when the strain and rotation are sufficiently small. However, such convergence study is missing in these existing works. To these ends, we consider the classical Eshelby's inclusion problem [22], owing to its crucial role in motivating the development of PFM as well as its wide applications in micromechanics of defects [21]. In particular, we consider a spherical inclusion that undergoes an inelastic (eigen) deformation, described by FST and SST as, respectively,

$$\mathbf{F}_i = \begin{bmatrix} 1 + \alpha/3 & \gamma & 0 \\ 0 & 1 + \alpha/3 & 0 \\ 0 & 0 & 1 + \alpha/3 \end{bmatrix} \quad (26)$$

$$\boldsymbol{\epsilon}^0 = \begin{bmatrix} \alpha/3 & \gamma/2 & 0 \\ \gamma/2 & \alpha/3 & 0 \\ 0 & 0 & \alpha/3 \end{bmatrix}$$

which represents a combined motion of a simple shear γ and an isotropic dilation α . Note that the infinitesimal strain tensor $\boldsymbol{\epsilon}^0$ clearly ignores the rotation associated with the simple shear in \mathbf{F}_i . For numerical implementation, a $128 \times 128 \times 128$ (regular) computational grid is used where a spherical inclusion with a normalized radius of 0.1 is placed in the center. (The interface is made slightly diffuse to avoid the Gibbs phenomenon.) Isotropic elasticity, with a shear modulus of 1000MPa and a Poisson's ratio of 0.3, is used for both the inclusion and matrix, which implies a homogeneous elastic medium leading to analytical solutions in the framework of SST. Using a fully clamped boundary condition with different values of α and γ in Eq. (26), we can solve the micromechanical fields to reveal the quantitative difference between SST and FST.

3.2.1. Shear-dilation coupling

A particular geometrically nonlinear effect to explore here is the *shear-dilation coupling*, i.e., the scenario of $\alpha \neq 0$ and $\gamma \neq 0$ in Eq. (26). We first consider the scenario of pure dilation, i.e., $\alpha > 0$ and $\gamma = 0$.

Figure 2(a) shows the σ_{xx} values along a probe line parallel to x -axis and across the center of the inclusion, together with the analytical solution of SST [23]. It is seen that for this pure dilation case, the SST and FST give rise to very similar results even for a 20% dilation. This agreement has actually been reported previously in [24], where the analytical solution from SST and the finite-element solution from FST show virtually identical stresses inside a spherical inclusion with an eigen dilation of 10%.

We then add a simple shear to the eigen deformation of the inclusion, i.e., $\alpha > 0$ and $\gamma > 0$. The small strain analytical solution of this case is simply a linear superposition of the individual solution of the pure dilation and pure shear cases, which turn out to be independent of each other. As a result, introducing a non-zero γ to $\boldsymbol{\epsilon}^0$ in Eq. (26) should not change the solutions of diagonal stress components as predicted by SST. This is indeed confirmed by our numerical calculation. However, our calculation using FST predicts a quite different result, as shown in Fig. 2(b). It is seen that by adding a simple shear to the eigen deformation, the symmetry of the stress, namely, $\sigma_{xx} = \sigma_{yy} = \sigma_{zz}$ in the previous pure dilation scenario, is clearly broken, leading to a shear-dilation coupling. This result is obviously a manifestation of the geometric nonlinearity in the FST based micromechanics and may have some significant physical implications. For instance, it suggests that a simple shear may actually modify the diffusion potential (depending mainly on the diagonal stress components) of point defects, challenging the conventional idea that diffusion is mainly controlled by the hydrostatic pressure.

3.2.2. Convergence study

A series of calculations for different values of the eigen-strain (with $\alpha = \gamma$) are further carried out as a convergence analysis. In particular, we plot the predicted σ_{xx} at the center of the inclusion against the eigen-strain value in Fig. 3(a), which shows that a linear relationship between the stress and strain is predicted by SST but a nonlinear one by FST (owing to the shear-dilation coupling presented previously). The relative difference is further plotted against the eigen-strain value in Fig. 3(b), which suggests that the relative error (due to the small strain assumption) shows roughly a linear dependence on the eigen-strain value. Note that when the eigen-strain value is small enough, the shear-dilation coupling effect becomes negligible as well.

4. Model application to microstructure evolution: Deformation twinning

We choose deformation twinning (DT) as an example to demonstrate the application of the current PFM theory to modeling the dynamic coupling between micromechanical and microstructural evolution. While several PF models of DT have been developed

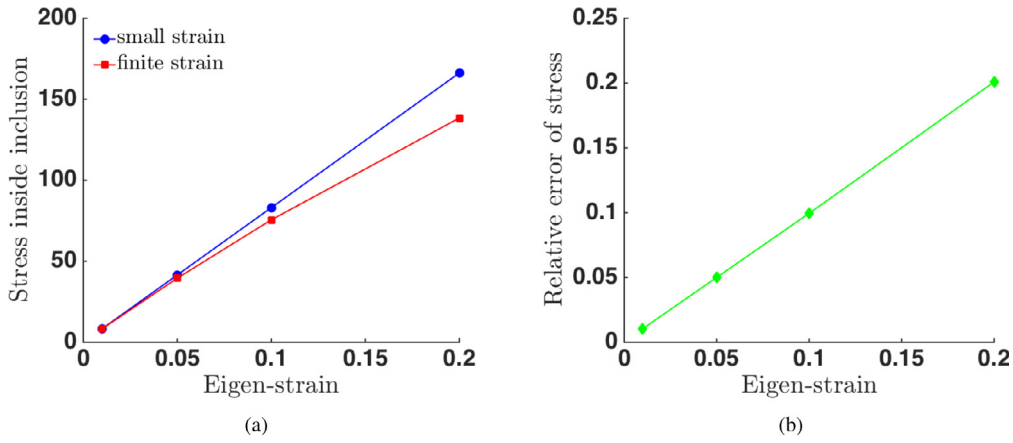


Fig. 3. (a) Predicted σ_{xx} value at the center of the inclusion versus the eigen-strain value ($\alpha = \gamma$). (b) Relative error of the small strain micromechanical solver with respect to the finite strain solver.

previously [25–28], they all used SST and were mainly limited to the study of DT in 2D. [29] developed a PF model of DT at finite strains, but the numerical implementation was still limited to 2D and the error due to SST was not studied. [7] recently developed an integrated PF model with crystal plasticity to study DT in magnesium, but the focus was again on 2D implementation. In fact, most experimental and theoretical/modeling studies on DT so far are limited to 2D and the underlying 3D features have just been started to resolve recently [30–34]. Nevertheless, the typically ultra-fast growth kinetics of DT is still a significant challenge for the experimental study.

While the DT can involve complex atomistic mechanisms [35,36], the overall shape of the growing twins, from a mesoscopic energy perspective, may be effectively determined by the competition between the elastic and interfacial energies. So long as the elastic strain fields associated with the twinning shear is largely maintained before significant recovery and hence the loss of coherency stress of DT, it is expected that the 3D shape of DT should be such that it minimizes the total internal energy consisting of mainly the elastic and interfacial energies. In addition, a recent high-resolution digital image correlation (DIC) study in magnesium has shown clearly that DT can occur in regions both with and without prior slips and suggested the important role played by the *local* stress states on DT [37]. Thus a DT model containing only the elastic and interfacial energies without plasticity can still bear some physical significance. In what follows, we present 3D simulations of the growth of $\{1\ 0\ \bar{1}\ 2\} \langle \bar{1}\ 0\ 1\ 1 \rangle$ DT in magnesium, focusing on (i) the 3D shape of the twin at early growth stages and (ii) the difference between using SST and FST based PF models.

4.1. Constitutive equations

In the PF model, a single crystal undergoing DT is described by the OP field η_0 , which is equal to 0 inside the matrix, 1 inside the twin, and between 0 and 1 at interface. Since only the reference configuration is involved in the following model development, in what follows we will ignore the subscript “0” of variables as long as the context is clear. In addition to the general constitutive equations (Section 2.2.1) associated with the current PFM theory, the inelastic deformation \mathbf{F}_i needs to be specified for DT,

$$\mathbf{F}_i = \left(1 - \sum_p \phi(\eta_p)\right) \mathbf{I} + \sum_p \phi(\eta_p) \mathbf{F}_i^{(p)}, \quad (27)$$

$$\mathbf{F}_i^{(p)} = \mathbf{I} + \gamma_{dt} \mathbf{s}_p \otimes \mathbf{m}_p,$$

where \mathbf{s}_p and \mathbf{m}_p are unit vectors of, respectively, the twinning shear direction (η_1 direction) and twinning plane (K_1 plane) normal of the

p -th twin variant, $\mathbf{F}_i^{(p)}$ is the deformation gradient associated with the twinning shear, and N_v is the total number of twin variants. The interpolation function $\phi(\eta)$ takes the form $\phi(\eta) = 3\eta^2 - 2\eta^3$ following [29] and the characteristic shear γ_{dt} for $\{1\ 0\ \bar{1}\ 2\} \langle \bar{1}\ 0\ 1\ 1 \rangle$ DT is given as [38]

$$\gamma_{dt} = \frac{\sqrt{3}a}{c} - \frac{c}{\sqrt{3}a} \quad (28)$$

where c and a are the lattice constants of the HCP structure of magnesium. In the current study, we use $c = 0.521\text{nm}$ and $a = 0.321\text{nm}$, which gives $\gamma_{dt} = 0.1301$. Note that Eq. (27) provides the coupling between \mathbf{F}_i and the OP, which is required in the diffuse-interface model. The linear coupling of Eq. (27) is a simple (and commonly used) form that ensures that \mathbf{F}_i becomes the eigen deformation $\mathbf{F}_i^{(p)}$ inside the DT. If the actual transformation strain pathway is determined by atomistic calculations, nonlinear coupling forms may be needed as shown in [39]. Nevertheless, it needs to be pointed out that Eq. (27) does not impair the geometric nonlinearity of the current model, which is inherited from the finite deformation framework used in Section 2.1. To complete the constitutive description, the inelastic Helmholtz free energy of Eq. (10) needs to be specified for DT, which is given as (an extension of [29])

$$\begin{aligned} \Psi_i &= \Psi_i^c + \Psi_i^g \\ &= \int_{V_0} \sum_p \left(A_1 \eta_p^2 (1 - \eta_p)^2 + \sum_{q \neq p} A_2 \eta_p^2 \eta_q^2 \right) dV_0 + \int_{V_0} \sum_p \kappa^{(p)} \\ &: \left(\nabla \eta_p \otimes \nabla \eta_p \right) dV_0 \end{aligned} \quad (29)$$

where A_1 and A_2 are two constants and $\kappa^{(p)}$ is a second-rank tensor related to anisotropic interfacial energies. In the integrand of Ψ_i^c , the first term is a double-well potential, which represents the *equal* internal energy states (i.e., $\eta = 0$ and $\eta = 1$) occupied by the parent and twin crystals, separated by an energy penalty associated with the interface; the second term is an energy penalty to prevent different variants from occupying the same space other than the interfaces. In principle, A_1 and $\kappa^{(p)}$ are determined by the equilibrium interfacial energy Δ and thickness l of an unstressed matrix/twin interface. (Note that for simplicity we restrict the formulation of gradient energy term in the reference configuration to avoid the configuration change as discussed in Section 2.2.2.) Following the treatment of [29], with the isotropic approximation we have $A_1 = \frac{12\Delta}{l}$ and $\kappa = \frac{3\Delta l}{4}$. A_2 is related to the unstressed interface between twin variants, the property of which are not commonly reported. Nevertheless, the primary focus of the current study is the growth of a single variant and the term related to A_2 is thus irrelevant.

4.2. Model parameters and dimensionless forms

To completely determine the model parameters for numerical implementation of the constitutive equation Eq. (29), the physical length of the computational grid must be specified. Given the increment of one grid point corresponding to l_0 (assuming the grid is evenly spaced along all three Cartesian axes), we can write the dimensionless form of Eq. (29) as

$$\Psi_{\dot{\mathbf{i}}}^* = \frac{\Psi_{\dot{\mathbf{i}}}}{A_1 l_0^3} = \int_{V_0} \left[\sum_p \left(A_1 \eta_p^2 (1 - \eta_p)^2 + \sum_{q \neq p} A_2 \eta_p^2 \eta_q^2 \right) + \sum_p \kappa^{(p)*} : (\nabla^* \eta_p \otimes \nabla^* \eta_p) \right] dV_0^* \quad (30)$$

where the dimensionless quantities (denoted by a superscript *) are defined in Table 2. Using the experimentally measured twin boundary energy $\Lambda = 0.117 \text{ J/m}^2$ [40] and a twin boundary thickness $l = 1 \text{ nm}$, we obtain $A_1 = 1.404 \text{ GPa}$. To fully determine the dimensionless quantities in Table 2, the grid spacing l_0 needs to be specified as well. Note that a characteristic length $l_c \equiv \sqrt{\kappa/A_1} = l/4$ can be defined such that the dimensionless gradient energy coefficient becomes $\kappa^* = (l_c/l_0)^2$. Since l_c is only 0.25 nm if the equilibrium twin boundary thickness is 1 nm , the choice of l_0 is then limited to nanometer scale as well. The elastic constants are taken as $c_{11} = 66.6 \text{ GPa}$, $c_{12} = 28.0 \text{ GPa}$, and $c_{44} = 19.3 \text{ GPa}$ by assuming isotropic elasticity, for single crystal magnesium is nearly elastically isotropic [29].

Finally the correspondence between the 3D computational grid and the crystallographic direction must be specified. We choose the following correspondence $\hat{x} \parallel \langle \bar{1}2\bar{1}0 \rangle$ ($\eta_1 \times K_1$), $\hat{y} \parallel \langle \bar{1}011 \rangle$ (η_1), $\hat{z} \parallel \langle 10\bar{1}2 \rangle$ (K_1), such that the inelastic deformations $\mathbf{F}_{\dot{\mathbf{i}}}^{(p)}$ associated with the two DT variants are

$$\mathbf{F}_{\dot{\mathbf{i}}}^{(1)} = \begin{bmatrix} 1 & 0 & 0 \\ 0 & 1 & 0.1301 \\ 0 & 0 & 1 \end{bmatrix}, \quad (31)$$

$$\mathbf{F}_{\dot{\mathbf{i}}}^{(2)} = \mathbf{R} \mathbf{F}_{\dot{\mathbf{i}}}^{(1)} \mathbf{R}^T = \begin{bmatrix} 1 & 0 & 0 \\ 0 & 0.9916 & 0.0005 \\ 0 & -0.1295 & 1.0084 \end{bmatrix},$$

where \mathbf{R} is given by (see Fig. 1 of [28] for the relevant crystallography)

$$\mathbf{R} = \begin{bmatrix} 1 & 0 & 0 \\ 0 & \cos\omega & \sin\omega \\ 0 & -\sin\omega & \cos\omega \end{bmatrix}, \quad \omega = -2 \arctan\left(\frac{c}{\sqrt{3}a}\right). \quad (32)$$

The corresponding gradient energy coefficient tensors are

$$\kappa^{(1)*} = \kappa^* \begin{bmatrix} 1 & 0 & 0 \\ 0 & 1 & 0 \\ 0 & 0 & 0.25 \end{bmatrix}, \quad (33)$$

$$\kappa^{(2)*} = \mathbf{R} \kappa^{(1)*} \mathbf{R}^T = \kappa^* \begin{bmatrix} 1 & 0 & 0 \\ 0 & 0.2532 & 0.0486 \\ 0 & 0.0486 & 0.9968 \end{bmatrix}.$$

4.3. Results

We use a $128 \times 128 \times 128$ computational grid with $l_0 = 0.5 \text{ nm}$ (leading to $\kappa^* = 0.25$), which implies a physical size of $64 \text{ nm} \times 64 \text{ nm} \times 64 \text{ nm}$ that is comparable with the typical size of twins at the early growth stage [37,41]. We ignore the complexity related to twin nucleation and simply introduce a small ellipsoidal region of DT in the initial configuration of the simulation as a stable nucleus. Under a constant applied shear stress $\tau = 2.5 \text{ GPa}$ along the η_1 direction, the twin nucleus is continuously growing in the 3D simulation. Note that the $\sim \text{GPa}$ level applied stress should be interpreted as the local stress (over a volume of $\sim 10^5 \text{ nm}^3$) that is necessary in order to drive the nanoscale twin to grow, which has also been shown in atomistic simulations [42] and is similar to the stress needed for homogeneous nucleation of dislocation loops. In reality, such high local stresses may be reasonably achieved in the vicinity of structural defects such as dislocations and grain boundaries.

Figure 4 presents the simulation results using FST based PF simulations, where snapshots in both 3D and 2D representations are shown. (For the purpose of comparing with the results of SST, the reference configuration is used to plot the OP field in Fig. 4.) Another PF simulation using SST is also carried out and the results are shown in Fig. 5 as a comparison with Fig. 4.

It is shown that the predicted DT processes are roughly the same for both SST and FST based PF simulations, especially in terms of the size and the overall morphological features of the twin. Both show that the twin initially adopts a roughly circular plate shape with the broad face closely parallel to K_1 , gradually develops into a roughly ellipsoidal plate with two unequal elliptic radii in K_1 , and eventually forms an infinite flat twin plate rigorously parallel to K_1 due to the usage of periodic boundary condition (PBC). A closer inspection suggests that before an infinite plate is formed, the broad face of the twin plate predicted by FST is not exactly aligned with K_1 whereas the broad face predicted by SST remains perfectly parallel to K_1 during the entire growth simulation. (Note that since the twin plate has varying thicknesses across K_1 , we define the broad face plane as the central plane.) This deviation from K_1 is particularly indicated by the snapshots of FST at $t^* = 120$ in Figs. 4(a) and 4(b), which exhibit ridges at the boundaries as the impingement due to PBC takes place. In contrast, no ridge is formed in the case of SST (Fig. 5), suggesting a perfect alignment of the broad face with K_1 . The presence of ridges is further demonstrated by the resulting significant local elastic distortion, which is shown by the elastic energy density fields plotted in Fig. 6. It is also interesting to compare the transformation kinetics predicted by SST and FST, which is shown in Fig. 7(a). Apparently there is little difference in terms of the evolution of DT volume fraction, which suggests that SST based PF simulations may still give an accurate prediction of the growth kinetics of DT (and likely other structural transformations such as martensitic transformation [39]).

A more detailed analysis of the shape of the twin and the comparison between results of SST and FST are shown in Fig. 8. The twin shows an overall lens-like shape, with one cross-section having a shape of

Table 2
Physical quantities and their dimensionless forms used in the current phase-field model.

Physical quantity [unit]	Dimensionless form	Definition
\mathbf{X} [m]	$\mathbf{X}^* = \mathbf{X}/l_0$	Material point vector
∇ [1/m]	$\nabla^* = \nabla * l_0$	Gradient operator
A_1 [J/m ³]	$A_1^* = 1$	Chemical free energy parameter
A_2 [J/m ³]	$A_2^* = 10$	Chemical free energy parameter
κ [J/m]	$\kappa^* = \kappa/(A_1 l_0^2)$	Isotropic gradient term coefficient
\mathbf{c} [J/m ³]	$\mathbf{c}^* = \mathbf{c}/A_1$	Elastic stiffness tensor
Ψ_e [J]	$\Psi_e^* = \Psi_e/(A_1 l_0^3)$	Elastic part of Helmholtz free energy
$\Psi_{\dot{\mathbf{i}}}$ [J]	$\Psi_{\dot{\mathbf{i}}}^* = \Psi_{\dot{\mathbf{i}}}/(A_1 l_0^3)$	Inelastic part of Helmholtz free energy

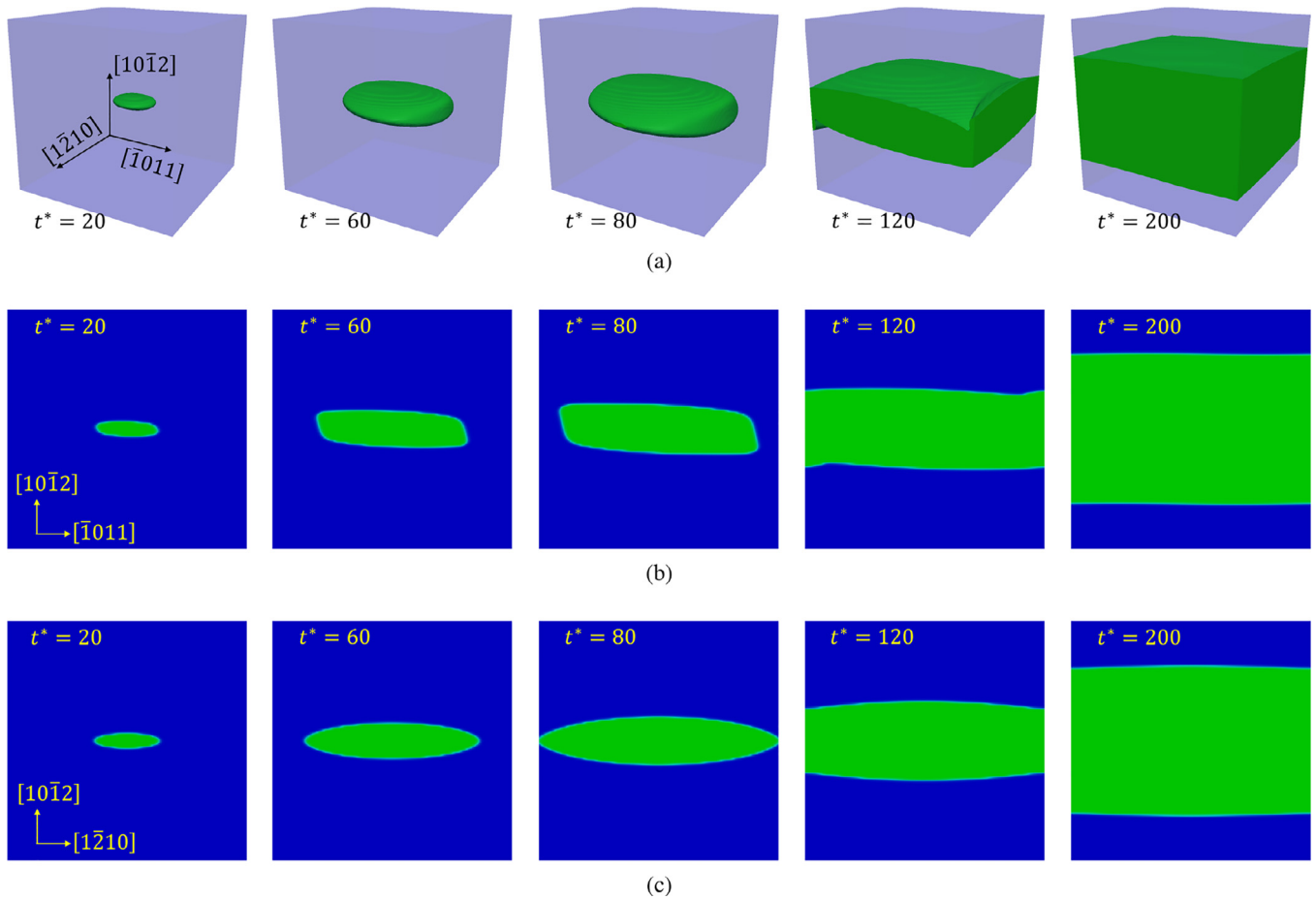


Fig. 4. Simulation snapshots in (a) 3D and (b–c) 2D representations showing the growth of a deformation twin (green region) using FST, where t^* indicates the reduced time in the PF simulations and the plots are in the current configuration. (For interpretation of the references to color in this figure legend, the reader is referred to the web version of this article.)

parallelogram with rounded corners and the other two cross-sections having ellipse shapes. This confirms that the speculated twin shape in [32] may indeed be physical. In addition, our PF simulation shows more detailed features of twin morphology. As shown by the 2D contour plots in Fig. 8, a lenticular shape is obtained when the twin is projected on to the plane normal to η_1 , which is referred to as the “dark side” of twin in [32] (because it cannot be resolved using conventional experimental techniques). The top view (cross-section normal to K_1) of the twin is predicted to be an ellipse and predictions from SST and FST are quite similar to each other. However, the “bright side” (cross-section normal to $\eta_1 \times K_1$) of the twin, which corresponds to the typical 2D experimental characterization, only shows a lenticular-like plate but with blunt tips for both SST and FST. However, experimental images of deformation twins terminated inside grains do show sharp tips [43–45], and we will discuss this discrepancy in more details later in Section 4.4. Nevertheless, it is obvious that the central plane of the twin plate (on the bright side) predicted by FST deviates from that predicted by SST; the latter is perfectly aligned with K_1 whereas the former deviates from K_1 by some angle θ . This is a subtle but critical feature that cannot be obtained using SST simulations and its physical origin will be explored next.

4.4. Discussion

4.4.1. Deviation of twin boundary from K_1

The angle θ between K_1 and the central plane of the twin plate is identified quantitatively in Fig. 9 (where owing to the viewing angle being precisely along $K_1 \times \eta_1$, the central planes appear as lines), which turns out to be 3.72° for FST and zero for SST.

We further carry out large-scale 2D simulations using a 1024×1024 computational grid parallel to $\{\bar{1}2\bar{1}0\}$ plane (normal to $\eta_1 \times K_1$), with exactly the same input parameters as those in the previous 3D simulations. The results from both SST and FST simulations are shown in Fig. 10. Owing to the much larger computational grid, the twin plate can grow without impingement (nor coalescence) up to $t^* = 400$ (twice as long as the previous 3D simulations). Because of the removal of finite size effect along the $\langle \bar{1}2\bar{1}0 \rangle$ (normal to the 2D computational grid), there is a slight difference in terms of the growth kinetics predicted by 2D and 3D simulations, as shown in Fig. 7(b). However, the twin shape predicted from the 2D simulation is essentially the same as that obtained from cross-sectioning the 3D result through the same plane. In particular, the deviation angle θ from K_1 in 2D FST simulation is again confirmed to be $\sim 3.72^\circ$, and remains the same during the entire simulation as shown in Fig. 10(b).

It is also interesting to carry out parametric studies to explore the influence of some model parameters on the value of θ . In particular, we are interested in the anisotropic ratio of interfacial energy, defined as $\zeta \equiv \kappa_{33}^*/\kappa_{11}^*$ in the principal coordinates (here using the gradient coefficient tensor for the first variant in Eq. (33)) and is set to be 0.25 in the previous 2D and 3D simulations. Since the simulated twin plate shape is a result of the competition between elastic and interfacial energies, changing the interfacial energy anisotropy is expected to significantly alter the twin plate shape when the elastic modulus is kept constant as a material property.

We use different values of ζ (1, 1/4, 1/8, and 1/16) to carry out a series of 2D simulations using both SST and FST, and the simulated twin shapes are compared in Fig. 11. Contour lines representing the shapes of the twins from SST and FST are superimposed upon each

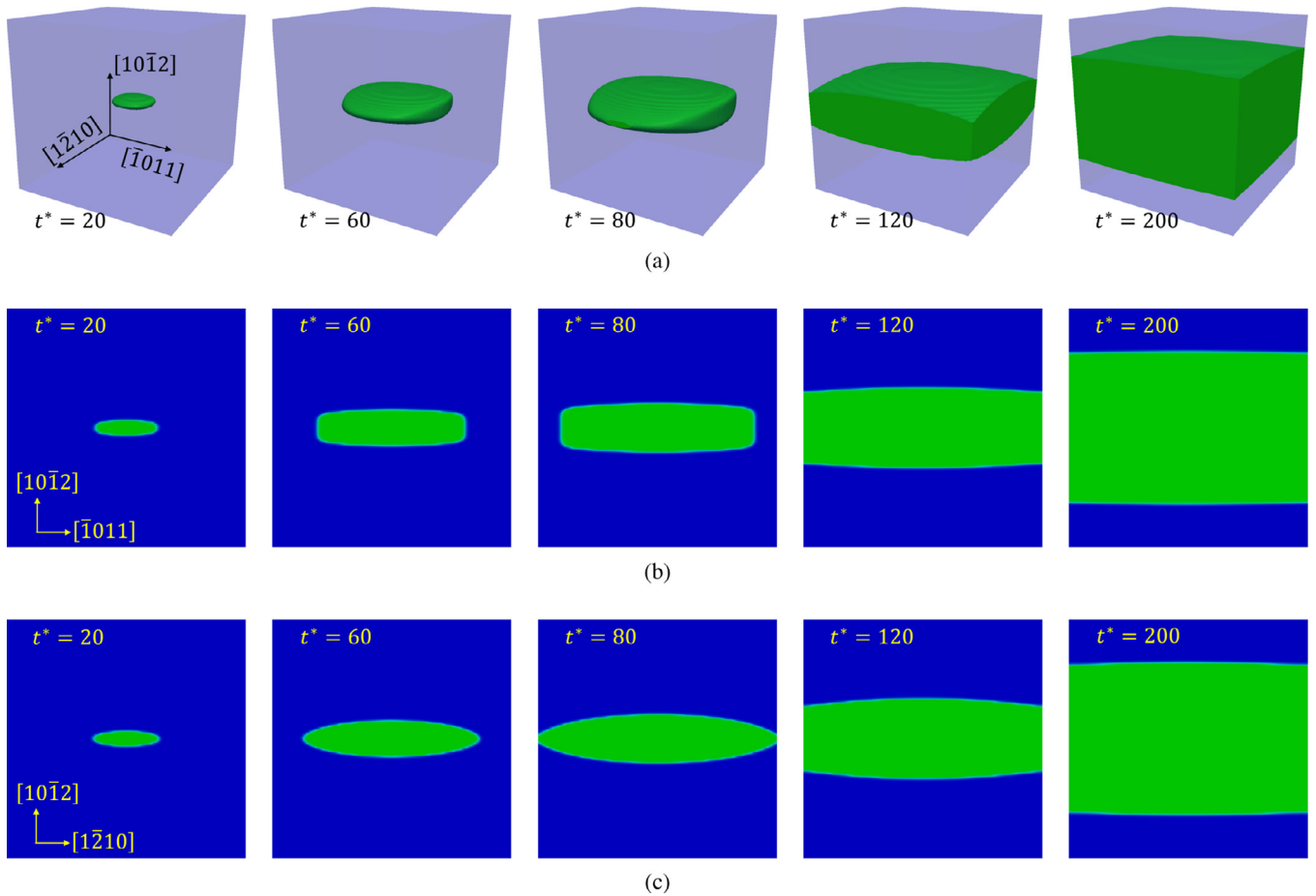


Fig. 5. Similar illustrations as in Fig. 4, but for the SST based PF simulations.

other in Fig. 11 for better comparison. In both cases, the aspect ratio of the twin plates show significant dependence on ζ , as summarized in Fig. 12(a). (Note that for a given ζ , the aspect ratio is confirmed to remain approximately constant with less than $\sim 3\%$ variation during the simulation, and is virtually the same for both SST and FST simulations.) As expected, a smaller ζ (i.e., higher interfacial energy anisotropy) leads to a larger aspect ratio of the twin plate; in the case of isotropic interfacial energy ($\zeta = 1$), an aspect ratio of 1 is obtained. In addition, it is obvious that the resulting aspect ratio can significantly influence θ for the FST simulations, as summarized in Fig. 12(b). (In contrast, no deviation from K_1 is observed in SST simulations

regardless of the aspect ratio of the twin plate.) As the aspect ratio increases, θ decreases and reaches zero when the twin plate adopts a sufficiently large aspect ratio, as shown in the case of $\zeta = 1/16$ in Fig. 11. A finite-sized twin plate with a smaller aspect ratio, i.e., a “thicker” twin, will possess a higher area fraction of the (blunt) twin tip. Since the twin tip interface cannot be an invariant plane and thus causes significant elastic distortions, the observed deviation θ from K_1 must be attributed to the tip effect. Indeed, as the aspect ratio increases, the twin becomes thinner and thinner, and thus possesses a lower area fraction of the twin tip, leading to a smaller and smaller and eventually vanishing θ .

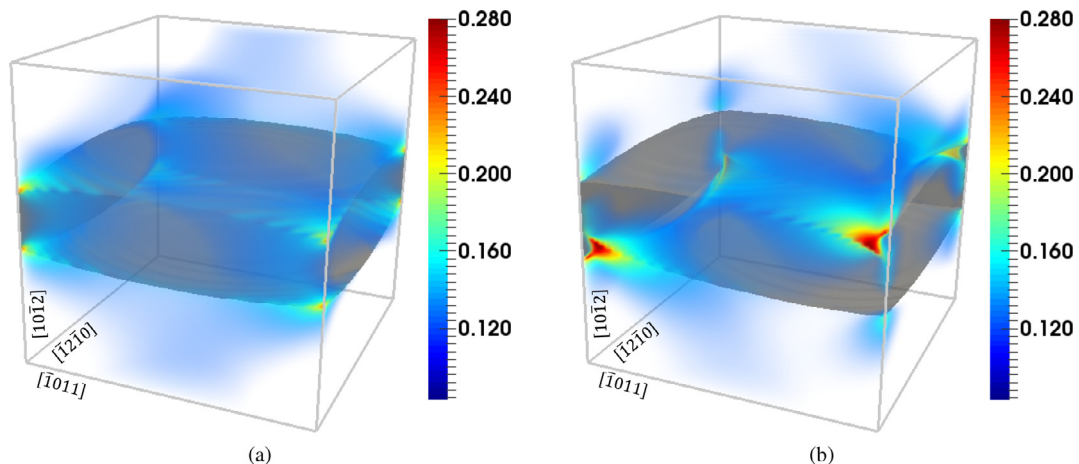


Fig. 6. Elastic energy density fields at $t^* = 120$ predicted from (a) SST and (b) FST simulations. The colorbars have the same scale range and are in units of A_1 (1.404GPa).

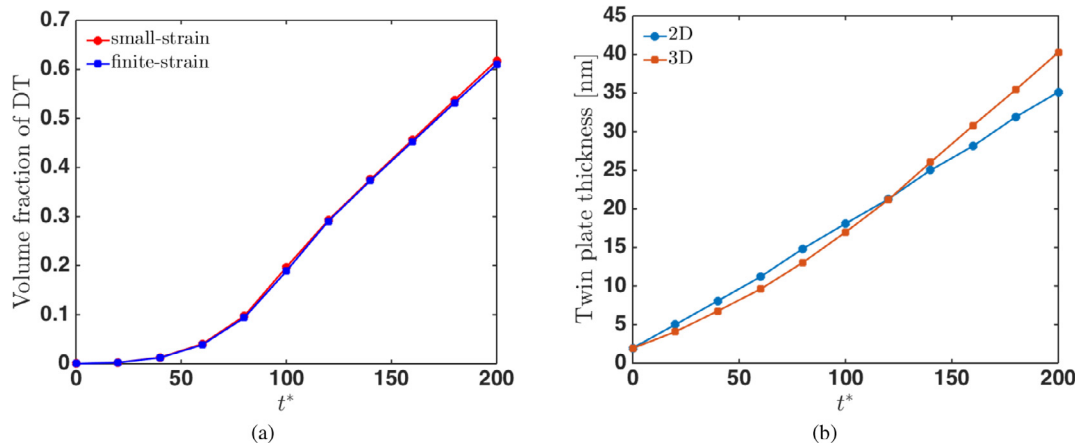


Fig. 7. Evolution of (a) DT volume fraction predicted from 3D simulations using SST and FST, and (b) DT thickness predicted from 2D and 3D simulations using SST.

4.4.2. Stress field asymmetry

Since the microstructural evolution of the DT is essentially controlled by the local stress field, the distinctive deviation from K_1 should be closely related to the different stress fields predicted by SST and FST. We compare the stress fields around the (finite-sized) twin plate predicted by 3D PF simulations using SST and FST. Figures 13 and 14 correspond to the 3D twin plate at $t^* = 60$ in Section 4.3. (Note that the 2D P-K stress is used here for comparison with the SST result.) Under the applied boundary condition, only four components, i.e., σ_{xx} , σ_{yy} , σ_{zz} , and σ_{yz} are non-zero for both SST and FST simulations. Comparing Figs. 13 and 14, the differences are readily seen.

First, even though both SST and FST predict that the maximum and minimum values of each stress components appear to be at the blunt tips of the twin, the distributed regions of these extreme values exhibit clearly different shapes. For σ_{xx} , σ_{yy} , and σ_{zz} predicted by SST, the maximum and minimum values simply equal in magnitude and differ by the sign, and their distributed regions show mirror symmetries about K_1 and the plane normal to η_1 as shown in Fig. 13. In contrast, σ_{xx} , σ_{yy} , and σ_{zz} predicted by FST show asymmetric magnitudes of the maximum and minimum values, and their distributed regions are clearly asymmetric without any mirror symmetry as shown in Fig. 14. It is interesting to point out that for these diagonal stress components around the deformation twin, FST predicts that the tensile states are higher in magnitude but more locally distributed, whereas the compressive states are lower in magnitude but more broadly distributed. This result is consistent with the fact that the volume average of σ_{xx} , σ_{yy} , and σ_{zz} must equal to zero, and may lead to some interesting physical implications such as asymmetric twin boundary structure development and different solute segregation at twin boundaries [46].

For the predictions of σ_{yz} , which is the only non-zero stress component applied externally, the qualitative difference in terms of the distributed symmetry of the extreme values is still seen in Figs. 13 and 14. To

be more quantitative, we plot σ_{yz} values along the two probe lines (solid and dashed) shown in Fig. 13 and 14, and the results are shown in Fig. 15. When the probe line is across the center of the twin plate, predictions of σ_{yz} from both SST and FST are close to each other as shown in Fig. 15(a). Note that the stress inside the twin plate is not constant as in the case of an ellipsoidal Eshelby's inclusion [22], but shows some variations in both SST and FST. This should be expected, because the simulated twin plate does not adopt an exact ellipsoidal shape.

As the probe line moves away from the twin plate, more significant differences between the predictions of σ_{yz} are present, as shown in Fig. 15(b). In particular, SST yields a symmetric variation of the σ_{yz} along the dashed probe line, whereas FST yields an asymmetric one, leading to a difference in the local values of σ_{yz} around the twin plate. In a recent experimental work by [47], it was shown that the stress field across a twin plate was indeed distributed asymmetrically; in addition, the plastic deformation was also found asymmetric across the twin plate, which was expected to be closely related to the stress asymmetry. The current DT model using FST allows to explore these asymmetries that may lead to asymmetric twin growth when plasticity is considered.

4.4.3. Effect of anisotropy in interface mobility

As we have pointed out earlier, the simulated twin plate, when projected on the bright side, always shows blunt tips (using both FST and SST). This is in contrast to the experimental characterization that always shows sharp tips when the twin is terminated inside a grain [43–45]. One critical assumption in the previous simulations is the usage of isotropic interface mobility (i.e., a constant M in Eq. (15)), which has also been used in all the previous PF models of DT [7,25–29,48]. However, numerous experimental observations have suggested that the lengthwise growth (i.e., along η_1) of deformation twins should occur much faster than the twin thickening (i.e., normal to K_1 plane). As a result, we hypothesize that the tapering of the

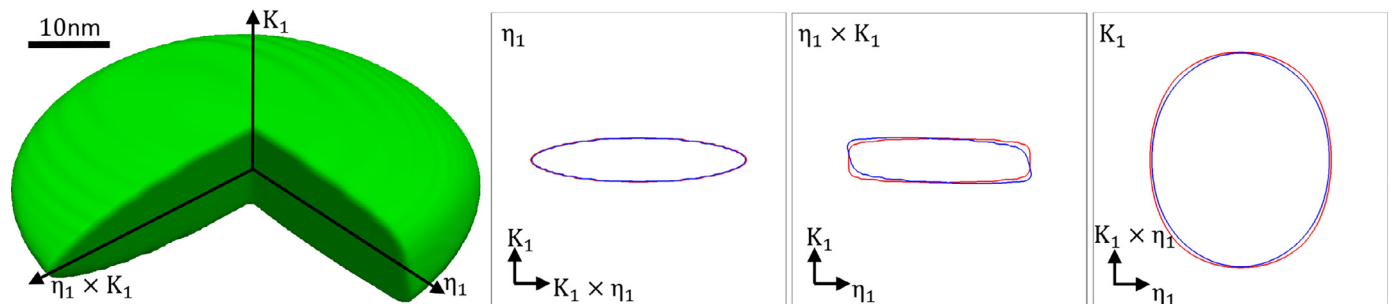


Fig. 8. 3D shape of a simulated deformation twin at the early growth stage using FST, together with the comparison between results from SST (red lines) and FST (blue lines) showing the boundary of twins (contour lines of order parameter equal to 0.5) on different cross-section planes as indicated. For interpretation of the references to color in this figure legend, the reader is referred to the web version of this article.)

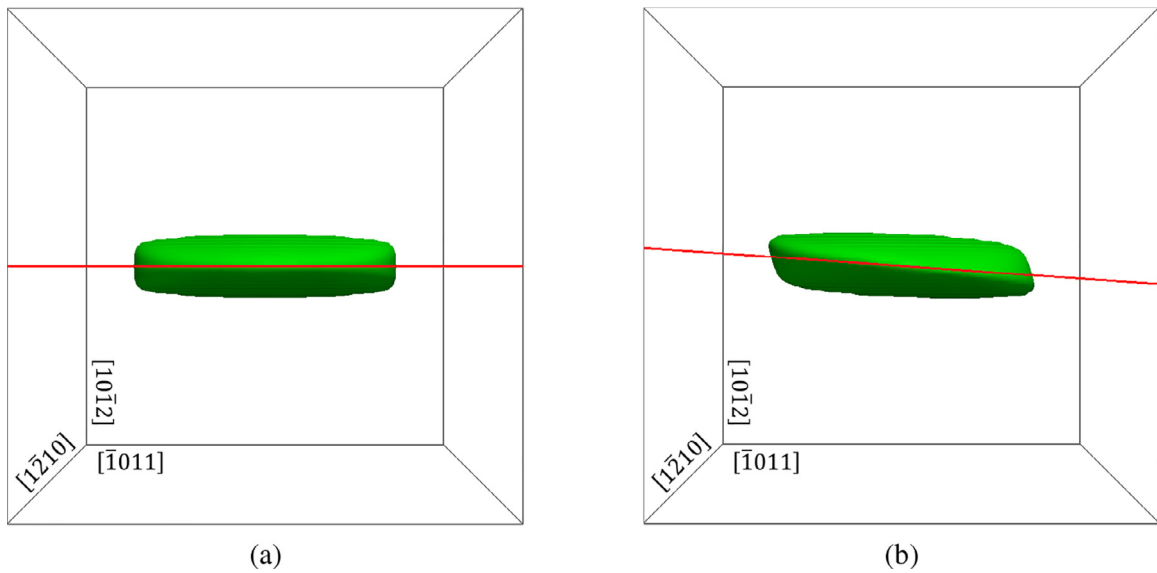


Fig. 9. Central planes (red lines) of the simulated twin plate using (a) SST and (b) FST. (For interpretation of the references to color in this figure legend, the reader is referred to the web version of this article.)

deformation twin tip may be due to the anisotropy in the twin interface mobility. The underlying physical basis is related to the twin boundary migration mechanisms and hence to the twin boundary structures. In terms of twin dislocation theory, the thickening process requires a production of additional twin dislocations at the twin interface, whereas the lengthwise growth is mainly controlled by the mobility of twin dislocations [49]. The dynamic theory associated with DT growth in magnesium is so far still an open question and currently under active studies [50–52]. To test our hypothesis, we introduce anisotropy in the interface mobility by making M in Eq. (15) location-dependent. More specifically, we propose the following mathematical expression for (reduced) interface mobility

$$M^* = M^*(\mathbf{X}) = M_1 + M_2 |\cos\beta|^n \quad (34)$$

where M_1 and M_2 are two (non-negative) constants, β is the angle between the twin/matrix interface normal and η_1 , and n is a positive

integer characterizing the variation of the β -dependent mobility. Obviously, the lengthwise growth along η_1 (i.e., $\beta = 0^\circ$ or 180°) is associated with the largest mobility of $M_1 + M_2$, the twin thickening (i.e., $\beta = 90^\circ$ or 270°) is associated with the smallest mobility of M_1 , and in between the mobility varies continuously. In principle, the value for M_1 and $M_1 + M_2$ can be obtained from atomistic simulations of the corresponding interface mobility, and the actual functional form for $M^*(\mathbf{X})$ can be constructed with calculations for more special interfaces instead of using the proposed Eq. (34). Here we focus on the hypothesis testing in a qualitative manner by assuming $n = 2$ and assigning different sets of values for M_1 and M_2 . The sets of parameters used in the subsequent 2D simulations are listed in Table 3.

The simulation results are shown in Fig. 16. It is obvious that the anisotropy in interface mobility can significantly change the shape of a growing twin for both SST and FST simulations. The tapering of the twin tip is indeed observed for all three anisotropic cases in Table 3

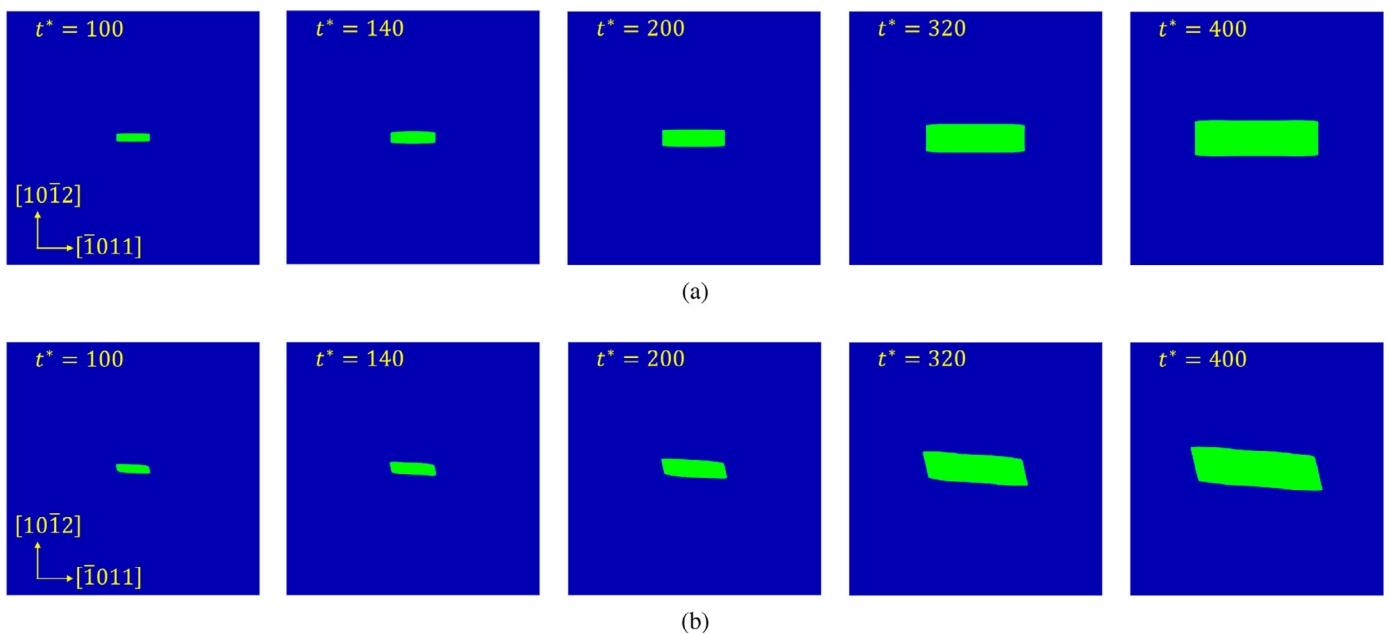


Fig. 10. Snapshots from 2D simulations using (a) SST and (b) FST, showing the growth of a deformation twin (green region). (For interpretation of the references to color in this figure legend, the reader is referred to the web version of this article.)

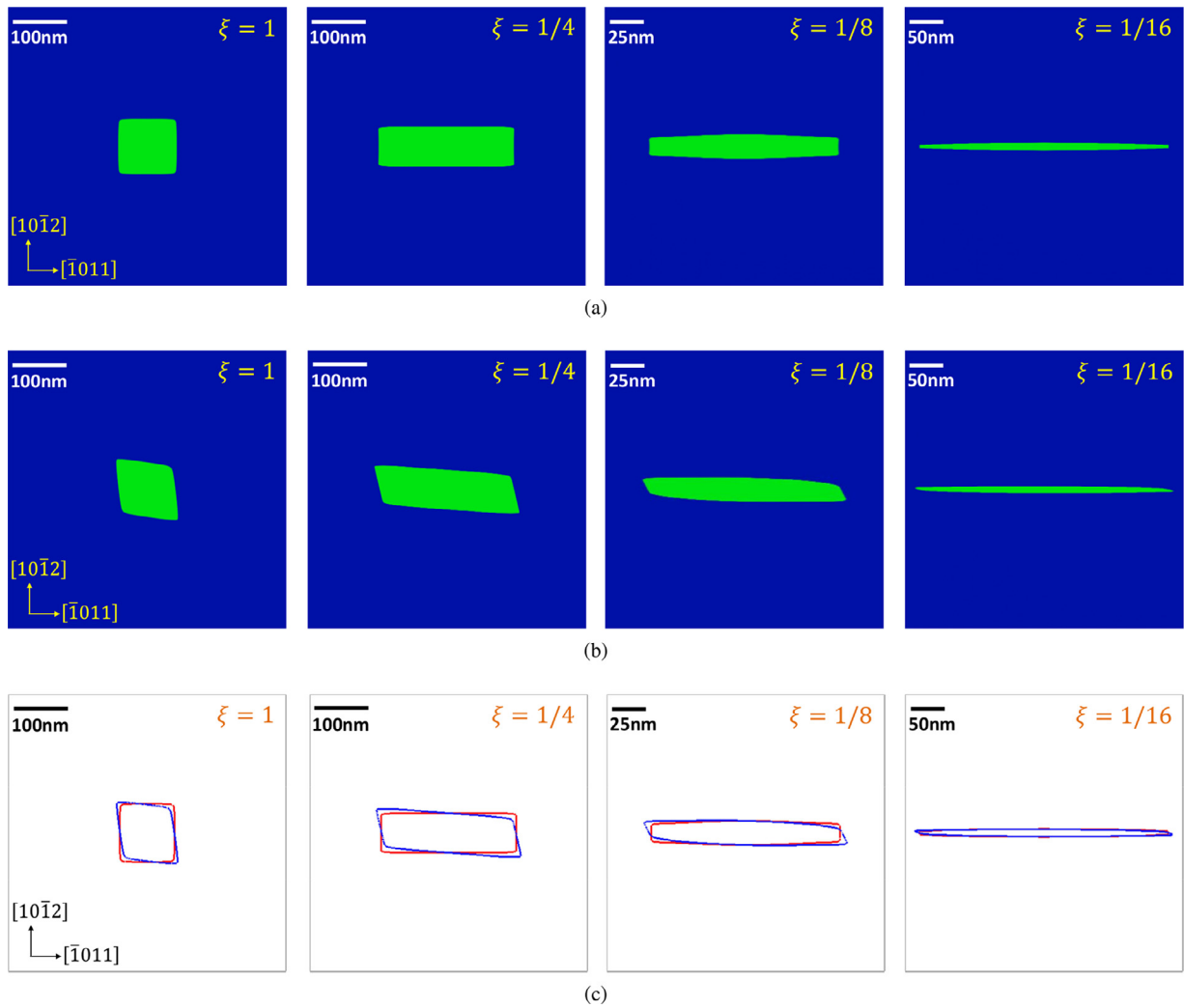


Fig. 11. Simulated deformation twin (green region) morphology using (a) SST and (b) FST with different interfacial energy anisotropy ξ , together with (c) the comparison between the twin boundaries represented by contour lines (of order parameter equal to 0.5, red for SST and blue for FST). (For interpretation of the references to color in this figure legend, the reader is referred to the web version of this article.)

(i.e., Set 2 to 4) using both SST and FST. In addition, the twin tip becomes sharper as the degree of anisotropy in the interface mobility increases, which will diminish the deviation from K_1 obtained in FST simulations and hence reduce the discrepancy between the results of

SST and FST. As a result, our parametric study confirms that the anisotropy in twin/matrix interface mobility can indeed produce very sharp twin tips as observed in the experiments. Since the shape of the DT is controlled by the asymmetry of the local stress field caused

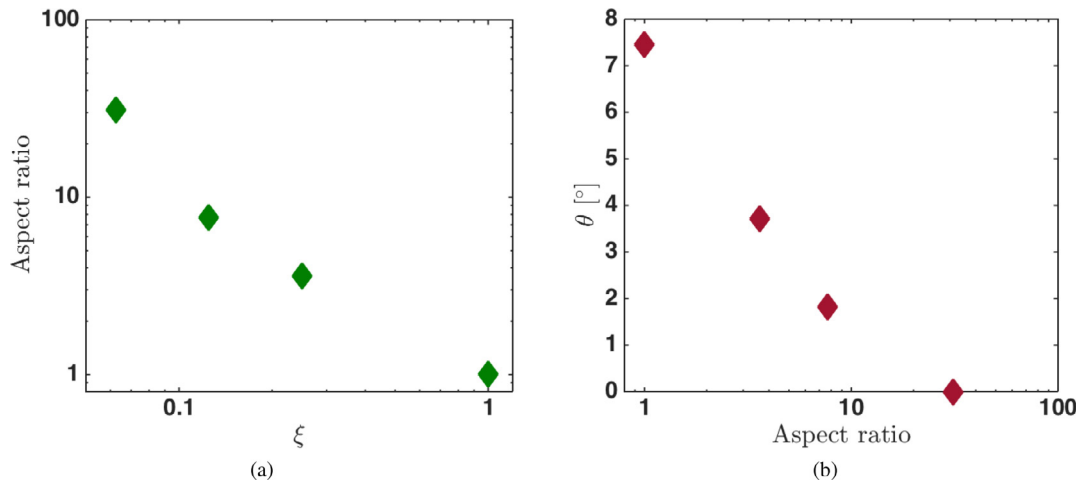


Fig. 12. (a) Dependence of the twin plate aspect ratio on the interfacial energy anisotropy ratio ξ . (b) Dependence of the deviation angle θ from K_1 (in FST simulations) on the twin plate aspect ratio.

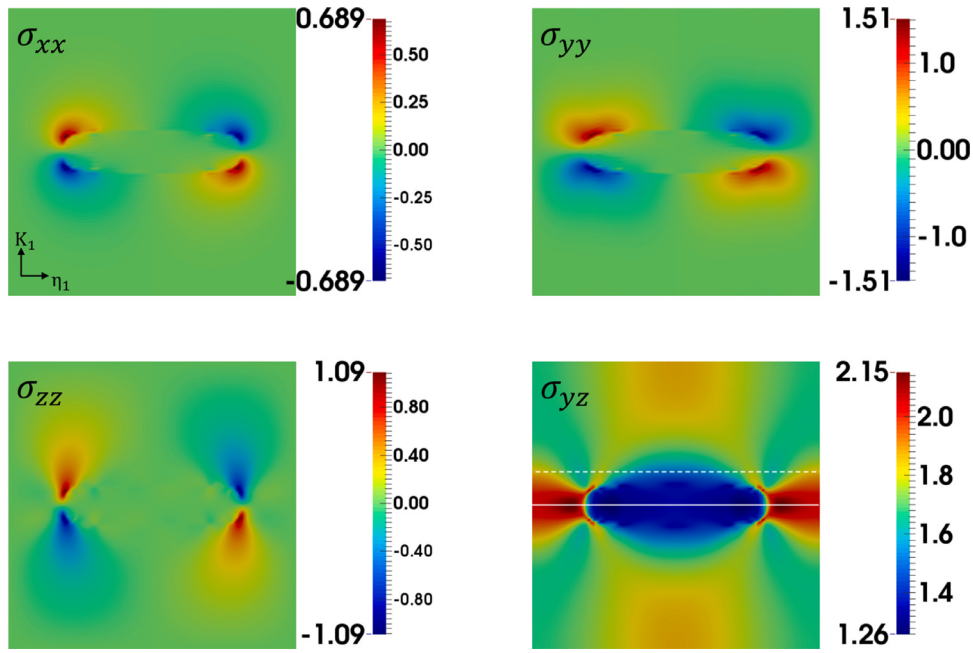


Fig. 13. Stress fields around a deformation twin predicted using SST. Cross-sections normal to $\eta_1 \times K_1$ are shown here and the unit of colorbar is A_1 (1.404GPa).

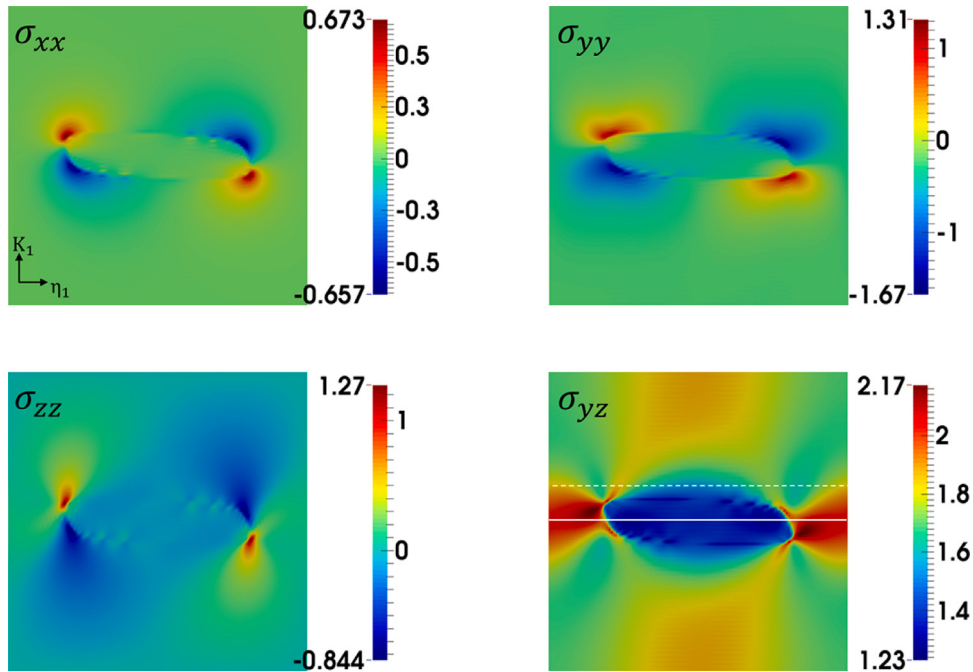


Fig. 14. Stress (2nd P-K stress) fields around the deformation twin predicted using FST. Cross-sections normal to $\eta_1 \times K_1$ are shown here and the unit of colorbar is A_1 (1.404GPa).

by the blunt tips, when the blunt tips are removed by the growth anisotropy, the deviation of twin boundary from K_1 vanishes. Thus, for a quantitative simulation of DT at mesoscale, the anisotropy in terms of both interface energy and mobility must be considered, which can be provided by atomistic simulations.

5. Conclusions

A phase-field microelasticity theory at finite strains is developed following Khachaturyan's classical work at small strains. The new theory is further incorporated into the general phase-field

framework of modeling microstructure evolution in solids, with the corresponding constitutive and evolution equations being rigorously derived following the thermodynamic consistency. Owing to the representation in the reference configuration, the current phase-field model at finite strains can be readily implemented using the micromechanical solver based on Fourier spectral method, which provides higher numerical efficiency as compared to conventional finite-element method based models. The calculation of the micromechanical field associated with a spherical Eshelby's inclusion is carried out as a benchmark study. A shear-dilatation coupling owing to the geometric nonlinearity is revealed,

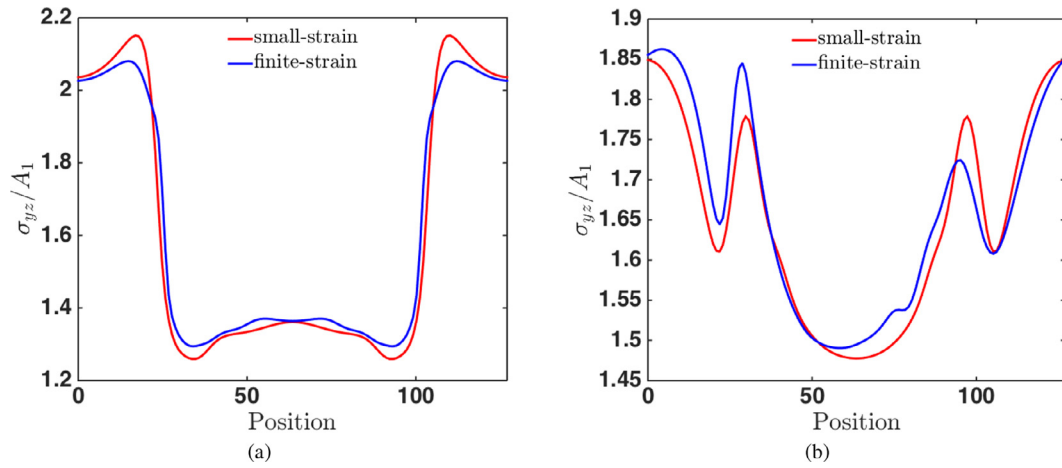


Fig. 15. σ_{yz} values along the (a) solid and (b) dashed lines shown in Figs. 13 and 14.

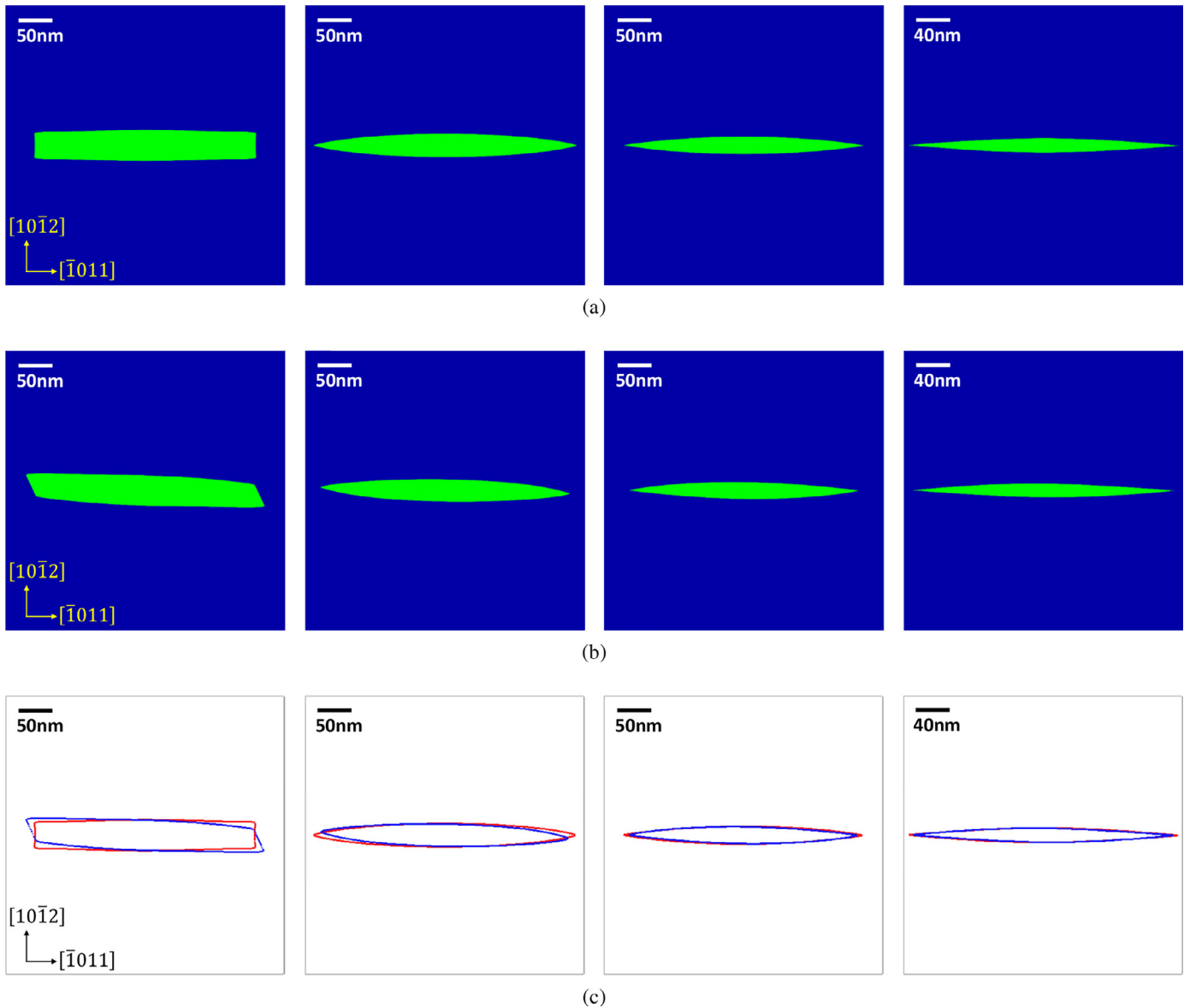


Fig. 16. Simulated deformation twin (green region) morphology using (a) SST and (b) FST with different anisotropy in interface mobility, together with (c) the comparison between the twin boundaries represented by contour lines (of order parameter equal to 0.5, red for SST and blue for FST). For each row, the images from left to right correspond to the parameter Set 1 to 4 in Table 3, with increasing the degree of anisotropy in interface mobility. (For interpretation of the references to color in this figure legend, the reader is referred to the web version of this article.)

Table 3
Different sets of parameters used for anisotropic interface mobility (Eq. (34)).

Set No.	M_1	M_2	Ratio of mobility between thickening and lengthwise growth
1	1.0	0.0	1.0 (isotropic case)
2	0.7	0.3	0.7
3	0.5	0.5	0.5
4	0.3	0.7	0.3

together with a convergence study to quantitatively compare our new theory with the conventional small strain theory.

The new theory is then applied to modeling the growth of $\{1\ 0\ \bar{1}\ 2\}\langle\bar{1}\ 0\ 1\ 1\rangle$ deformation twins in magnesium, which offers a rigorous and detailed comparison between small strain and finite strain predictions on the co-evolution of microstructural and micromechanical fields. A deviation of the twin/matrix boundary from the K_1 plane is predicted by the finite strain theory, which is, however, absent in the prediction by the small strain theory. Parametric studies are further carried out to confirm that this deviation is due to the tip effect when the twin plate has a finite size with a relatively low aspect ratio (corresponding to early stages of growth). As the aspect ratio increases (due to, e.g., higher interfacial energy anisotropy or growth anisotropy), the deviation decreases and eventually vanishes for an infinite twin plate, which is consistent with the classical crystallography theory. Asymmetric stress fields around the twin tip are also predicted by the finite strain phase-field simulations, whereas the small strain based simulations always predict symmetric stress field around the twin tip. The experimentally observed sharp twin tip is shown to be likely due to the anisotropy in the twin/matrix interface mobility, which originates from differences in interface structures and growth mechanisms and could be provided by atomistic simulations and high-resolution electron microscopy characterizations.

Declaration of interests

The authors declare that they have no known competing financial interests or personal relationships that could have appeared to influence the work reported in this paper.

Acknowledgments

This work is supported by the National Energy Technology Laboratory under Grant No. DE-FE0027776 and National Science Foundation under Grant No. DMREF 1534826 (P.Z., Y.W. and S.R.N.). The authors gratefully acknowledge the allocation of computing time from Ohio Supercomputer Center. The authors also thank the anonymous reviewers for their thoroughness and insightful comments.

Appendix A. General expression of the derivative of a functional of a functional

Let $\mathcal{F}[\phi]$ be a functional, i.e., a mapping from a normed linear space of functions (a Banach space) $M = \{\phi(x) : x \in \mathbb{R}\}$ to a field of real or complex numbers, $\mathcal{F} : M \rightarrow \mathbb{R}$ or \mathbb{C} . Now consider $\mathcal{G}[\mathcal{F}[\phi]]$, which is a functional of a functional. In the scenario of PFM in question, one can think of \mathcal{F} as the stress field, \mathcal{G} the total elastic energy, and ϕ the order parameter field. Then the driving force used in formulating the rate equation of $\dot{\phi}$ requires the functional derivative $\delta\mathcal{G}/\delta\phi$, which should be computed through the following chain rule

$$\frac{\delta}{\delta\phi(x)}\mathcal{G}[\mathcal{F}[\phi]] = \int_y dy \frac{\delta\mathcal{G}[\mathcal{F}]}{\delta\mathcal{F}(\phi(y))} \frac{\delta\mathcal{F}[\phi]}{\delta\phi(x)}. \quad (\text{A.1})$$

Eq. (A.1) is clearly different from the chain rule of the ordinary function of a function. To see why Eq. (A.1) holds, we may consider a set of N discretized points in \mathbb{R} , i.e., $\{x_1, x_2, \dots, x_N\}$, on which the field variables ϕ and \mathcal{F} take the sets of values $\{\phi_1, \phi_2, \dots, \phi_N\}$ and $\{f_1, f_2, \dots, f_N\}$, respectively. We then consider a function of many variables, $g = g(f_1, f_2, \dots, f_N)$ and each component f_i , $i = 1 \dots N$ is again a function of many variables, $f_i(\phi_1, \phi_2, \dots, \phi_N)$. Then according to the chain rule of ordinary functions, we can compute the following partial derivative

$$\frac{\partial g}{\partial\phi_i} = \sum_j^N \frac{\partial g}{\partial f_j} \frac{\partial f_j}{\partial\phi_i}. \quad (\text{A.2})$$

Taking the continuous limit of Eq. (A.2) by having $N \rightarrow \infty$ and replacing the summation with integration and the ordinary function with its functional counterpart, one can obtain Eq. (A.1) (a rigorous derivation can be found in the Appendix A of [53]). It is also seen that if \mathcal{F} is a localized functional (i.e., an ordinary function) of ϕ , then $\partial f_j / \partial\phi_i = 0$ for all $j \neq i$ in Eq. (A.2), which leads to a special case of Eq. (A.1)

$$\frac{\delta}{\delta\phi(x)}\mathcal{G}[\mathcal{F}[\phi]] = \frac{\delta\mathcal{G}[\mathcal{F}]}{\delta\mathcal{F}(\phi(x))} \frac{d\mathcal{F}[\phi]}{d\phi(x)}. \quad (\text{A.3})$$

Appendix B. Proof of additive decompositions in Table 1

We present here only the proof of one additive decomposition relation, i.e., $\mathbf{E}_e \equiv \mathbf{F}_i^T \bar{\mathbf{E}}_e \mathbf{F}_i = \mathbf{E} - \mathbf{E}_i$, as the proof of others can follow in a similar way. Starting with the definitions of three Green-Lagrange strain tensors defined in different configurations

$$\begin{aligned} \frac{1}{2}(|d\mathbf{x}|^2 - |d\mathbf{X}|^2) &= d\mathbf{X} \cdot \mathbf{E} \cdot d\mathbf{X}, \\ \frac{1}{2}(|d\bar{\mathbf{x}}|^2 - |d\mathbf{X}|^2) &= d\mathbf{X} \cdot \mathbf{E}_i \cdot d\mathbf{X}, \\ \frac{1}{2}(|d\mathbf{x}|^2 - |d\bar{\mathbf{x}}|^2) &= d\bar{\mathbf{x}} \cdot \bar{\mathbf{E}}_e \cdot d\bar{\mathbf{x}}, \end{aligned} \quad (\text{B.1})$$

we have

$$\begin{aligned} d\mathbf{X} \cdot \mathbf{E} \cdot d\mathbf{X} &= \frac{1}{2}(|d\mathbf{x}|^2 - |d\mathbf{X}|^2) = \frac{1}{2}(|d\mathbf{x}|^2 - |d\bar{\mathbf{x}}|^2 + |d\bar{\mathbf{x}}|^2 - |d\mathbf{X}|^2) \\ &= d\bar{\mathbf{x}} \cdot \bar{\mathbf{E}}_e \cdot d\bar{\mathbf{x}} + d\mathbf{X} \cdot \mathbf{E}_i \cdot d\mathbf{X} \\ &= (\mathbf{F}_i d\mathbf{X}) \cdot \bar{\mathbf{E}}_e \cdot (\mathbf{F}_i d\mathbf{X}) + d\mathbf{X} \cdot \mathbf{E}_i \cdot d\mathbf{X} \quad (\text{using } d\bar{\mathbf{x}} = \mathbf{F}_i d\mathbf{X}) \\ &= d\mathbf{X} \cdot (\mathbf{F}_i^T \bar{\mathbf{E}}_e \mathbf{F}_i) \cdot d\mathbf{X} + d\mathbf{X} \cdot \mathbf{E}_i \cdot d\mathbf{X} \\ &= d\mathbf{X} \cdot (\mathbf{F}_i^T \bar{\mathbf{E}}_e \mathbf{F}_i + \mathbf{E}_i) \cdot d\mathbf{X}. \end{aligned} \quad (\text{B.2})$$

In the derivation above, the use of $d\bar{\mathbf{x}} = \mathbf{F}_i d\mathbf{X}$ is based on the existence of the intermediate configuration as suggested by [17]. Clearly, by defining $\mathbf{E}_e \equiv \mathbf{F}_i^T \bar{\mathbf{E}}_e \mathbf{F}_i$ we have the following additive decomposition

$$\mathbf{E} = \mathbf{E}_e + \mathbf{E}_i. \quad (\text{B.3})$$

Appendix C. Mathematical proof of Eq. (16)

Based on Section 2.2.1, the total elastic strain energy in the reference configuration is formulated as

$$\begin{aligned} \Psi_e &= \int_{V_0} \rho_0 \psi_e dV_0 \\ &= \frac{1}{2} \int_{V_0} \bar{\mathbf{E}}_e(\mathbf{E}_e) : \mathbb{C} : \bar{\mathbf{E}}_e(\mathbf{E}_e) j_i dV_0 \\ &= \frac{1}{2} \int_{V_0} (\mathbf{F}_i^T \bar{\mathbf{E}}_e \mathbf{F}_i^{-1}) : \mathbb{C} : (\mathbf{F}_i^T \bar{\mathbf{E}}_e \mathbf{F}_i^{-1}) j_i dV_0. \end{aligned} \quad (\text{C.1})$$

In Eq. (C.1) $\bar{\mathbf{E}}_e(\mathbf{E}_e)$ should be interpreted as the pull-back function of the $\bar{\mathbf{E}}_e$ as specified in Table 1, such that the integration is still performed in the reference configuration. In addition, there is no restriction on $\bar{\mathbf{E}}_e$ (and hence \mathbf{E}_e) yet. If $\bar{\mathbf{E}}_e$ is obtained through solving the stress equilibrium equation in a static equilibrium problem, the corresponding Eq. C.1 gives the total elastic energy at mechanical equilibrium.

Suppose that we have obtained the equilibrium $\bar{\mathbf{E}}_e$, which, according to [1], is a functional of the OP field $\eta(\mathbf{X})$. In the PF method we will need to calculate the following functional derivative (which drives the system towards equilibrium)

$$\begin{aligned} \frac{\delta \Psi_e}{\delta \eta(\mathbf{X})} &= \int_{V_0} d^3 \mathbf{Y} \left\{ \frac{\delta \Psi_e}{\delta \bar{\mathbf{E}}_e(\mathbf{Y})} : \frac{\delta \bar{\mathbf{E}}_e(\mathbf{Y})}{\delta \eta(\mathbf{X})} \right\} \\ &= \int_{V_0} d^3 \mathbf{Y} \left\{ j_i(\mathbf{Y}) \bar{\mathbf{S}}(\mathbf{Y}) : \frac{\delta \bar{\mathbf{E}}_e(\mathbf{Y})}{\delta \eta(\mathbf{X})} \right\} \end{aligned} \quad (\text{C.2})$$

where the chain rule of a functional of a functional in Appendix A has been used. Note that we have ignored the dependence of j_i on \mathbf{F}_i (or η), since compared with $\bar{\mathbf{E}}_e(\eta)$, $j_i(\eta)$ can be considered as a slow functional of η and hence a secondary effect to the functional derivative. Physically this corresponds to the same assumption made for deriving Eq. (9) in Section 2.2.2, where the spatial variation of density function is small enough to be considered as constant. This treatment is well justified for dislocation plasticity and deformation twinning of metals where little voids and/or volume change are involved. While the stress field $\bar{\mathbf{S}}(\mathbf{X})$ can be obtained via numerical solutions of mechanical equilibrium, we still need an explicit functional expression for $\bar{\mathbf{E}}_e[\eta(\mathbf{X})]$ in order to continue the derivation in Eq. (C.2). Using the expression of $\bar{\mathbf{E}}_e = \mathbf{F}_i^{-T} \mathbf{E}_e \mathbf{F}_i^{-1}$ according to Table 1, we have

$$\begin{aligned} \frac{\delta \bar{\mathbf{E}}_e(\mathbf{Y})}{\delta \eta(\mathbf{X})} &= \int_{V_0} d^3 \mathbf{Y}' \left\{ \frac{\delta \bar{\mathbf{E}}_e(\mathbf{Y})}{\delta \mathbf{F}_i^{-T}(\mathbf{Y}')} : \frac{\delta \mathbf{F}_i^{-T}(\mathbf{Y}')}{\delta \eta(\mathbf{X})} + \frac{\delta \bar{\mathbf{E}}_e(\mathbf{Y})}{\delta \mathbf{E}_e(\mathbf{Y}')} : \frac{\delta \mathbf{E}_e(\mathbf{Y}')}{\delta \eta(\mathbf{X})} + \frac{\delta \bar{\mathbf{E}}_e(\mathbf{Y})}{\delta \mathbf{F}_i^{-1}(\mathbf{Y}')} : \frac{\delta \mathbf{F}_i^{-1}(\mathbf{Y}')}{\delta \eta(\mathbf{X})} \right\} \\ &= \left(\frac{d\mathbf{F}_i^{-T}(\mathbf{Y})}{d\eta} \cdot \mathbf{E}_e(\mathbf{Y}) \cdot \mathbf{F}_i^{-1}(\mathbf{Y}) \right) \delta(\mathbf{Y}-\mathbf{X}) + \mathbf{F}_i^{-T}(\mathbf{Y}) \cdot \frac{\delta \mathbf{E}_e(\mathbf{Y})}{\delta \eta(\mathbf{X})} \cdot \mathbf{F}_i^{-1}(\mathbf{Y}) \\ &\quad + \left(\mathbf{F}_i^{-T}(\mathbf{Y}) \cdot \mathbf{E}_e(\mathbf{Y}) \cdot \frac{d\mathbf{F}_i^{-1}(\mathbf{Y})}{d\eta} \right) \delta(\mathbf{Y}-\mathbf{X}) \end{aligned} \quad (\text{C.3})$$

where the coupling between η and \mathbf{F}_i is assumed to be given as a localized ordinary function as in the conventional PF methods. Substituting Eq. (C.3) together with the additive decomposition in Table 1 into Eq. (C.2), we have

$$\frac{\delta \Psi_e}{\delta \eta(\mathbf{X})} = -2\mathbf{S} : \left(\frac{d\mathbf{F}_i^{-T}}{d\eta} \mathbf{F}_i^{-T} \mathbf{E}_e \right) + \int_{V_0} d^3 \mathbf{Y} \left\{ \mathbf{S}(\mathbf{Y}) : \frac{\delta \mathbf{E}_e(\mathbf{Y})}{\delta \eta(\mathbf{X})} \right\} \quad (\text{C.4})$$

where the dependence on \mathbf{X} has been omitted so long as the context is clear. Using the additive decomposition $\mathbf{E}_e = \mathbf{E} - \mathbf{E}_i$ and definition of \mathbf{E}_i in Table 1, we have

$$\frac{\delta \mathbf{E}_e(\mathbf{Y})}{\delta \eta(\mathbf{X})} = \frac{\delta \mathbf{E}(\mathbf{Y})}{\delta \eta(\mathbf{X})} - \frac{1}{2} \left(\frac{d\mathbf{F}_i^{-T}}{d\eta} \mathbf{F}_i^{-T} \delta(\mathbf{Y}-\mathbf{X}) + \mathbf{F}_i^{-T} \frac{d\mathbf{F}_i}{d\eta} \delta(\mathbf{Y}-\mathbf{X}) \right). \quad (\text{C.5})$$

Substituting Eq. (C.5) in Eq. (C.4), we obtain

$$\begin{aligned} \frac{\delta \Psi_e}{\delta \eta(\mathbf{X})} &= -2\mathbf{S} : \left(\frac{d\mathbf{F}_i^{-T}}{d\eta} \mathbf{F}_i^{-T} \mathbf{E}_e \right) - \mathbf{S} : \left(\frac{d\mathbf{F}_i^{-T}}{d\eta} \mathbf{F}_i^{-T} \right) + \int_{V_0} d^3 \mathbf{Y} \left\{ \mathbf{S}(\mathbf{Y}) : \frac{\delta \mathbf{E}(\mathbf{Y})}{\delta \eta(\mathbf{X})} \right\} \\ &= -2\mathbf{S} : \left(\frac{d\mathbf{F}_i^{-T}}{d\eta} \mathbf{F}_i^{-T} (\mathbf{E} - \mathbf{E}_i) \right) - \mathbf{S} : \left(\frac{d\mathbf{F}_i^{-T}}{d\eta} \mathbf{F}_i^{-T} \right) + \int_{V_0} d^3 \mathbf{Y} \left\{ \mathbf{S}(\mathbf{Y}) : \frac{\delta \mathbf{E}(\mathbf{Y})}{\delta \eta(\mathbf{X})} \right\} \\ &= -\mathbf{F}_i^{-T} \mathbf{C} \mathbf{S} : \frac{d\mathbf{F}_i}{d\eta} + \int_{V_0} d^3 \mathbf{Y} \left\{ \mathbf{S}(\mathbf{Y}) : \frac{\delta \mathbf{E}(\mathbf{Y})}{\delta \eta(\mathbf{X})} \right\}. \end{aligned} \quad (\text{C.6})$$

The first term appears local and can be easily evaluated once the mechanical equilibrium is solved, physically corresponding to the effect due to the change of the inelastic deformation field. The second

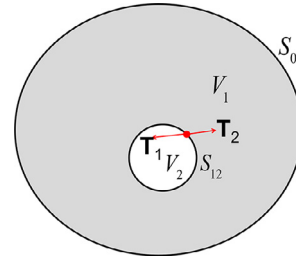


Fig. C.1. Schematics of an Eshelby type inclusion.

integral, at first glance, may likely be non-zero, as a local perturbation in microstructure ($\delta\eta$) can in principle result in non-local changes in the total displacement (and strain) and stress fields due to the long-range nature of elastic interaction. It turns out that this integral will be exactly zero when mechanical equilibrium is reached and the proof is as follows.

The second integral in Eq. (C.6) actually resembles the (negative) internal virtual work in the principle of virtual displacements, which, under static equilibrium, is written in the reference configuration as

$$\int_{S_0} \bar{\mathbf{T}} \cdot \delta \boldsymbol{\chi} dS + \int_{V_0} \mathbf{B} \cdot \delta \boldsymbol{\chi} dV = \int_{V_0} \mathbf{S} : \delta \mathbf{E} dV \quad (\text{C.7})$$

where $\bar{\mathbf{T}}$ is the traction applied on the surface S_0 , \mathbf{B} is the body force (per unit volume), $\delta \boldsymbol{\chi}$ and $\delta \mathbf{E}$ are the kinematically admissible virtual displacement and strain fields, respectively. Note that we have taken into account the difference between reference and intermediate configurations due to the multiplicative decomposition of Eq. (2).

The principle of virtual displacements, however, cannot be directly applied to the Eshelby's inclusion type problem, which is a paradigm of microstructural and micromechanical modeling, owing to the discontinuity in the stress field at the surface of the inclusion. As a result, we divide the whole configuration into two parts, V_1 and V_2 as illustrated in Fig. C.1. On the surface S_{12} that connects the two subbodies, V_1 experiences a traction of \mathbf{T}_1 and V_2 experiences a traction of \mathbf{T}_2 . Obviously, stress and displacement fields are all continuous in individual subbodies. We then apply Eq. (C.7) to both V_1 and V_2 :

$$\begin{aligned} \int_{S_{12}} \mathbf{T}_1 \cdot \delta \boldsymbol{\chi}_1 dS &= \int_{V_1} \mathbf{S} : \delta \mathbf{E} dV \\ \int_{S_{12}} \mathbf{T}_2 \cdot \delta \boldsymbol{\chi}_2 dS &= \int_{V_2} \mathbf{S} : \delta \mathbf{E} dV \end{aligned} \quad (\text{C.8})$$

where we have considered case with no body force prescribed and the outer surface S_0 at infinity is assumed stress-free. Since \mathbf{T}_1 and \mathbf{T}_2 must be equal and opposite by Newton's Third Law, we can combine the two equations into

$$\int_{S_{12}} \mathbf{T}_2 \cdot (\delta \boldsymbol{\chi}_2 - \delta \boldsymbol{\chi}_1) dS = \int_{V_0} \mathbf{S} : \delta \mathbf{E} dV_0. \quad (\text{C.9})$$

It needs to be emphasized that \mathbf{E} is the total strain associated with the kinematically admissible displacement field. Eq. (C.9) suggests that the quantity $\int_{V_0} \mathbf{S} : \delta \mathbf{E} dV$ (negative internal virtual work) in an Eshelby's inclusion problem subject to a virtual displacement field depends on the virtual displacement jump across the inclusion surface. If the applied virtual displacement field is continuous, i.e., $\delta \boldsymbol{\chi}_2 = \delta \boldsymbol{\chi}_1$, then we have

$$\int_{V_0} \mathbf{S} : \delta \mathbf{E} dV_0 = 0. \quad (\text{C.10})$$

In PFM theory (Section 2.2), the total strain \mathbf{E} is a functional of order parameter η and a microstructure change $\delta\eta$ will result in a variation of total strain $\delta\mathbf{E}$. By dividing $\delta\eta$ on both sides of Eq. (C.10) and taking the limit, we have

$$\int_{V_0} d^3 \mathbf{Y} \left\{ \mathbf{S}(\mathbf{Y}) : \frac{\delta \mathbf{E}(\mathbf{Y})}{\delta \eta(\mathbf{X})} \right\} = 0 \quad (\text{C.11})$$

which leads to the desired Eq. (16). Therefore, so long as the displacement at the inclusion/matrix interface maintains continuous (i.e., no gap or sliding is allowed), the virtual displacements in Eq. (C.9) have to satisfy $\delta\chi_2 = \delta\chi_1$ due to the kinematic admissibility and consequently Eq. (16) should be valid when the phase transformation and/or plastic deformation do not trigger any failure mechanism.

References

- [1] A.G. Khachaturyan, *Theory of Structural Transformations in Solids*, John Wiley & Sons, 1983.
- [2] L.-Q. Chen, Phase-field models for microstructure evolution, *Annual Review of Materials Research* 32 (1) (2002) 113–140.
- [3] Y. Wang, J. Li, Phase field modeling of defects and deformation, *Acta Materialia* 58 (4) (2010) 1212–1235.
- [4] V.I. Levitas, V.A. Levin, K.M. Zingerman, E.I. Freiman, Displacive phase transitions at large strains: phase-field theory and simulations, *Physical Review Letters* 103 (2) (2009) 025702.
- [5] F. Hildebrand, C. Miehe, A phase field model for the formation and evolution of martensitic laminate microstructure at finite strains, *Philosophical Magazine* 92 (34) (2012) 4250–4290.
- [6] A. Vattré, C. Denoual, Polymorphism of iron at high pressure: a 3D phase-field model for displacive transitions with finite elastoplastic deformations, *Journal of the Mechanics and Physics of Solids* 92 (2016) 1–27.
- [7] C. Liu, P. Shanthraj, M. Diehl, F. Roters, S. Dong, J. Dong, W. Ding, D. Raabe, An integrated crystal plasticity–phase field model for spatially resolved twin nucleation, propagation, and growth in hexagonal materials, *International Journal of Plasticity* 106 (2018) 203–227.
- [8] A. Finel, Y.L. Bouar, A. Gaubert, U. Salman, Phase field methods: Microstructures, mechanical properties and complexity, *Comptes Rendus Physique* 11 (3) (2010) 245–256. *Computational metallurgy and scale transitions*
- [9] L.N. Trefethen, *Spectral methods in MATLAB*, 10, SIAM, 2000.
- [10] P. Eisenlohr, M. Diehl, R.A. Lebensohn, F. Roters, A spectral method solution to crystal elasto-viscoplasticity at finite strains, *International Journal of Plasticity* 46 (2013) 37–53.
- [11] E. Borukhovich, P. Engels, T. Böhlke, O. Shchyglo, I. Steinbach, Large strain elastoplasticity for diffuse interface models, *Modelling and Simulation in Materials Science and Engineering* 22 (3) (2014) 034008.
- [12] E. Borukhovich, P.S. Engels, J. Mosler, O. Shchyglo, I. Steinbach, Large deformation framework for phase-field simulations at the mesoscale, *Computational Materials Science* 108 (2015) 367–373.
- [13] V.I. Levitas, D.L. Preston, Thermomechanical lattice instability and phase field theory of martensitic phase transformations, twinning and dislocations at large strains, *Physics Letters A* 343 (1–3) (2005) 32–39.
- [14] V.I. Levitas, Phase field approach to martensitic phase transformations with large strains and interface stresses, *Journal of the Mechanics and Physics of Solids* 70 (2014) 154–189.
- [15] M. Ambati, R. Kruse, L. De Lorenzis, A phase-field model for ductile fracture at finite strains and its experimental verification, *Computational Mechanics* 57 (1) (2016) 149–167.
- [16] P.P. Castaneda, P. Suquet, *Nonlinear composites*, *Advances in applied mechanics*, 34, Elsevier, 1997, pp. 171–302.
- [17] E.H. Lee, Elastic-plastic deformation at finite strains, *Journal of Applied Mechanics* 36 (1) (1969) 1–6.
- [18] F. Roters, P. Eisenlohr, L. Hantcherli, D.D. Tjahjanto, T.R. Bieler, D. Raabe, Overview of constitutive laws, kinematics, homogenization and multiscale methods in crystal plasticity finite-element modeling: Theory, experiments, applications, *Acta Materialia* 58 (4) (2010) 1152–1211.
- [19] A.E. Green, P.M. Naghdi, A general theory of an elastic-plastic continuum, *Archive for rational mechanics and analysis* 18 (4) (1965) 251–281.
- [20] Y. Wang, A. Khachaturyan, Three-dimensional field model and computer modeling of martensitic transformations, *Acta Materialia* 45 (2) (1997) 759–773.
- [21] T. Mura, *Micromechanics of defects in solids*, Springer Science & Business Media, 2013.
- [22] J.D. Eshelby, The determination of the elastic field of an ellipsoidal inclusion, and related problems, *Proceedings of the Royal Society of London. Series A. Mathematical and Physical Sciences* 241 (1226) (1957) 376–396.
- [23] A.F. Bower, *Applied Mechanics of Solids*, CRC press, 2009.
- [24] J.L. Diani, D. Parks, Problem of an inclusion in an infinite body, approach in large deformation, *Mechanics of materials* 32 (1) (2000) 43–55.
- [25] S. Hu, C.H. Henager Jr, L. Chen, Simulations of stress-induced twinning and detwinning: a phase field model, *Acta Materialia* 58 (19) (2010) 6554–6564.
- [26] T.W. Heo, Y. Wang, S. Bhattacharya, X. Sun, S. Hu, L.-Q. Chen, A phase-field model for deformation twinning, *Philosophical Magazine Letters* 91 (2) (2011) 110–121.
- [27] R. Kondo, Y. Tadano, K. Shizawa, A phase-field model of twinning and detwinning coupled with dislocation-based crystal plasticity for hcp metals, *Computational Materials Science* 95 (2014) 672–683.
- [28] H. Liu, F. Lin, P. Zhao, N. Moelans, Y. Wang, J. Nie, Formation and autocatalytic nucleation of co-zone {10 $\bar{1}$ 2} deformation twins in polycrystalline Mg: A phase field simulation study, *Acta Materialia* 153 (2018) 86–107.
- [29] J.D. Clayton, J. Knap, A phase field model of deformation twinning: nonlinear theory and numerical simulations, *Physica D: Nonlinear Phenomena* 240 (9–10) (2011) 841–858.
- [30] S. Yi, I. Schestakow, S. Zaefferer, Twinning-related microstructural evolution during hot rolling and subsequent annealing of pure magnesium, *Materials Science and Engineering: A* 516 (1–2) (2009) 58–64.
- [31] A. Fernández, A. Jérusalem, I. Gutiérrez-Urrutia, M. Pérez-Prado, Three-dimensional investigation of grain boundary–twin interactions in a Mg AZ31 alloy by electron backscatter diffraction and continuum modeling, *Acta Materialia* 61 (20) (2013) 7679–7692.
- [32] Y. Liu, N. Li, S. Shao, M. Gong, J. Wang, R. McCabe, Y. Jiang, C. Tomé, Characterizing the boundary lateral to the shear direction of deformation twins in magnesium, *Nature communications* 7 (2016) 11577.
- [33] M. Gong, J.P. Hirth, Y. Liu, Y. Shen, J. Wang, Interface structures and twinning mechanisms of twins in hexagonal metals, *Materials Research Letters* 5 (7) (2017) 449–464.
- [34] M. Gong, G. Liu, J. Wang, L. Capolungo, C.N. Tomé, Atomistic simulations of interaction between basal <a> dislocations and three-dimensional twins in magnesium, *Acta Materialia* 155 (2018) 187–198.
- [35] A. Luque, M. Ghazisaeidi, W.A. Curtin, A new mechanism for twin growth in Mg alloys, *Acta Materialia* 81 (2014) 442–456.
- [36] A. Ishii, J. Li, S. Ogata, Shuffling-controlled versus strain-controlled deformation twinning: The case for HCP Mg twin nucleation, *International Journal of Plasticity* 82 (2016) 32–43.
- [37] A. Orozco-Caballero, D. Lunt, J.D. Robson, J.Q. da Fonseca, How magnesium accommodates local deformation incompatibility: a high-resolution digital image correlation study, *Acta Materialia* 133 (2017) 367–379.
- [38] W.F. Hosford, *Mechanical behavior of materials*, Cambridge University Press, 2010.
- [39] P. Zhao, C. Shen, J. Li, Y. Wang, Effect of nonlinear and noncollinear transformation strain pathways in phase-field modeling of nucleation and growth during martensite transformation, *npj Computational Materials* 3 (1) (2017) 19.
- [40] J. Wang, J. Hirth, C. Tomé, {10 $\bar{1}$ 2} twinning nucleation mechanisms in hexagonal-close-packed crystals, *Acta Materialia* 57 (18) (2009) 5521–5530.
- [41] Q. Yu, Z.-W. Shan, J. Li, X. Huang, L. Xiao, J. Sun, E. Ma, Strong crystal size effect on deformation twinning, *Nature* 463 (7279) (2010) 335.
- [42] C. Barrett, H. El Kadiri, M. Tschopp, Breakdown of the schmid law in homogeneous and heterogeneous nucleation events of slip and twinning in magnesium, *Journal of the Mechanics and Physics of Solids* 60 (12) (2012) 2084–2099.
- [43] L. Wang, P. Eisenlohr, Y. Yang, T. Bieler, M. Crimp, Nucleation of paired twins at grain boundaries in titanium, *Scripta Materialia* 63 (8) (2010) 827–830.
- [44] F. Wang, S. Sandlöbes, M. Diehl, L. Sharma, F. Roters, D. Raabe, In situ observation of collective grain-scale mechanics in Mg and Mg–rare earth alloys, *Acta Materialia* 80 (2014) 77–93.
- [45] Q. Yu, J. Wang, Y. Jiang, R.J. McCabe, N. Li, C.N. Tomé, Twin–twin interactions in magnesium, *Acta Materialia* 77 (2014) 28–42.
- [46] J. Nie, Y. Zhu, J. Liu, X.-Y. Fang, Periodic segregation of solute atoms in fully coherent twin boundaries, *Science* 340 (6135) (2013) 957–960.
- [47] A. Kumar, M.B. Clausen, L. Capolungo, R.J. McCabe, W. Liu, J.Z. Tischler, C.N. Tomé, Deformation twinning and grain partitioning in a hexagonal close-packed magnesium alloy, *Nature Communications* 9 (1) (2018) 4761.
- [48] Z. Pi, Q. Fang, B. Liu, H. Feng, Y. Liu, Y. Liu, P. Wen, A phase field study focuses on the transverse propagation of deformation twinning for hexagonal-close packed crystals, *International Journal of Plasticity* 76 (2016) 130–146.
- [49] M. Yoo, J. Lee, Deformation twinning in hcp metals and alloys, *Philosophical Magazine* A 63 (5) (1991) 987–1000.
- [50] B. Xu, L. Capolungo, D. Rodney, On the importance of prismatic/basal interfaces in the growth of {10 $\bar{1}$ 2} twins in hexagonal close packed crystals, *Scripta Materialia* 68 (11) (2013) 901–904.
- [51] Q. Zu, X.-Z. Tang, S. Xu, Y.-F. Guo, Atomistic study of nucleation and migration of the basal/prismatic interfaces in Mg single crystals, *Acta Materialia* 130 (2017) 310–318.
- [52] F. Wang, C.D. Barrett, R.J. McCabe, H. El Kadiri, L. Capolungo, S.R. Agnew, Dislocation induced twin growth and formation of basal stacking faults in {10 $\bar{1}$ 2} twins in pure Mg, *Acta Materialia* 165 (2019) 471–485.
- [53] E. Engel, R.M. Dreizler, *Density functional theory*, Springer, 2013.